University of South Bohemia in České Budějovice

Faculty of Science

Bachelor's thesis

Characterizing the Impact of the SARS-CoV-2 British Mutation on Mouse Lung Tissue Using 3D SBF-SEM Imaging

Laboratory of Electron Microscopy

Coroianu Ana Maria

Supervisor: Týč Jiří, RNDr., Ph.D.

Co-supervisor: Marie Vancová, RNDr., Ph.D.

České Budějovice, 2024

Coroianu, A.M., 2024: Characterizing the Impact of the SARS-CoV-2 British Mutation on Mouse Lung Tissue Using 3D SBF-SEM Imaging. Bc. Thesis, in English, 42 pages, Faculty of Science, University of South Bohemia, České Budějovice, Czech Republic.

Annotation: This thesis investigates ultrastructural changes in mouse lungs after infection of the severe acute respiratory syndrome Coronavirus 2 (SARS-CoV-2), the causative agent of the global COVID-19 pandemic. Focusing on the British SARS-CoV-2 B.1.1.7 variant, the research aims to identify and describe what is happening in the infected lung tissue during the early infection stages. By analyzing serial block face scanning electron microscopy (SBF-SEM) datasets at three time points, the thesis aims to contribute insights into the onset and the progression of the disease.

Declaration:

I declare that I am the author of this qualification thesis and that in writing it I have used the sources and literature displayed in the list of used sources only.

České Budějovice, date

……

Coroianu Ana-Maria

Acknowledgments

I would like to express my sincere gratitude to my supervisor, Týč Jiří, RNDr., Ph.D., for his invaluable guidance and expertise throughout the research process. I am also thankful to my co-supervisor, Marie Vancová, RNDr., Ph.D., for her patient guidance and insightful feedback. Aditionally, I extend my appreciation to the entire Laboratory of Electron Microscopy team for their assistance and collaboration, which contributed to the completion of this study. Lastly, I am profoundly grateful to my and fiancé, my sister and friends for their constant support, unwavering encouragement, and patience.

Abstract

In December 2019, the severe acute respiratory syndrome Coronavirus 2 (SARS-CoV-2), the causative agent of COVID 19 disease, emerged, identified by the World Health Organization (WHO). This event has led to a global pandemic, resulting in over 770 million infections and almost seven million deaths. This unprecedented threat to public health has prompted extensive research into the evolution of the virus. In our study, we aimed to investigate the progression of the COVID 19 disease from healthy lungs to infected ones, with a specific focus on the impact of the British SARS-CoV-2 mutation, known as the B.1.1.7 variant, in mouse lungs. Sample preparation involved processing mouse lung tissues for serial block face scanning electron microscopy (SBF SEM). This process included fixation, staining, dehydration, infiltration, embedding, polymerization, and mounting for SBF SEM observation. Analysis of SBF SEM datasets of healthy lung cells, lung cells on the second day post-infection, and those on the fifth day post-infection revealed substantial changes and disease progression. Notably, the number of pro-inflammatory macrophage cells of the immune system increased by 2,5% on the second day of infection. Additionally, the count of necrotic cells increased to 0,45%, while on the fifth day, it further rose to 0,8%. This thesis presents a detailed analysis of the SBF SEM images stacked into data sets, focusing on the primary objective of understanding the impact of the SARS-CoV-2 B.1.1.7 variant on infected lungs.

Table of Contents

List of abbreviations

ACE 2 – Angiotensin converting enzyme

ARDS - acute respiratory distress syndrome

COVID 19 – Coronavirus disease 2019

EC- endothelial cells

EM - Electron Microscopy

GB – Gigabyte

MERS-CoV- Middle East Respiratory Syndrome Coronavirus 1

MIB - Microscopy Image Browse

NLC- Negative Lung Control

ROIs – Regions of interest

SARS-CoV-1- Severe Acute Resipiratory Syndrome Coronavirus 1

SARS-CoV-2 – severe acute respiratory syndrome coronavirus 2

SBF-SEM – Serial block face scanning electron microscopy

SEM - Scanning electron microscope

WHO – World Health Organization

1. Introduction

1.1 SARS-CoV-2 and Human's Health

From the beginning of December 2019 according to the World Health Organization (WHO), the first case of the Coronavirus of severe acute respiratory syndrome (SARS-CoV-2) was identified and it has rapidly spread causing more than 770 million infections and almost seven million deaths worldwide representing a threat to human's health. (WHO, COVID-19, 2020) According to Khaswal et. All (2022), the disease is recognized for causing permanent harm in some patients, which is expected to result in various degrees of health issues, ranging from mild to severe. Notably, other coronaviruses such as SARS-CoV-1 (Severe Acute Respiratory Syndrome Coronavirus 1), and MERS-CoV (Middle East Respiratory Syndrome Coronavirus 1) have also been associated with permanent damage. SARS- CoV-1 was first identified in 2002 in the province of China and led to the SARS outbreak, resulting in severe respiratory illness with a mortality rate of 10% while MERS-CoV was first reported in 2012 in Saudi Arabia, characterized by respiratory symptoms and mortality rate of 35%. (Pormohammad et. al, 2020) In addition to the evident lung damage caused by these infections, individuals who have survived COVID-19 exhibit a wide range of dysfunctions in different organ systems, similar to what is seen in SARS-CoV-1 and MERS cases. The manifestations of SARS-CoV-2 primarily affect the respiratory system, with symptoms such as cough, fever and shortness of breath being the most prominent. However, the virus also exhibits long-term effects on various organ systems, including the central nervous system, cardiovascular system, pulmonary system, gastrointestinal system, hematologic system, renal system, and psycho-social aspects. SARS-CoV-2 leads to the manifestation of the disease in these organs and their related systems in a significant number of recovered cases (Kashwal et. al, 2022). Recent evidence, as highlighted by a retrospective study in China (Mao et al. 2020), suggests that COVID-19 may impact the nervous system. Some COVID-19 patients experienced neurological symptoms, including impaired consciousness, muscle problems, and cerebrovascular issues. Severe cases were more likely to exhibit these symptoms, and some patients also reported symptoms like loss of smell and taste (hyposmia and hypogeusia). However, at the time of the study by Li et all, the link between these symptoms and patient outcomes remained unestablished. In the same group of patients, another study (Li et al. 2020 a, b) revealed that 13 individuals who had COVID-19 experienced acute cerebrovascular diseases,

such as cerebral hemorrhage and ischemic stroke. These conditions were more prevalent in older patients and those with severe disease. A study in France (Helms et al. 2020) involving COVID-19 patients with acute respiratory distress syndrome reported similar neurological manifestations in 85% of cases, leading to various medical interventions. (Jha et. al, 2021; Li Y et. al. 2020; Li YC et. al, 2020; Li Y et. al. 2004; Mao L et. all, 2020). Furthermore, SARS-CoV-2 has experienced genetic mutations that significantly impact its pathogenesis during the COVID-19 pandemic. Various strains of the virus, such as D614G, B.1.1.7 (United Kingdom), B.1.1.28 (Brazil P1, P2), CAL.20C (Southern California), B.1.351 (South Africa), B.1.617 (B.1.617.1 Kappa & Delta B.1.617.2), and B.1.1.529 (Omicron), have emerged globally. These mutations, particularly within the receptor-binding domain (RBD) of the spike (S) protein, are pivotal in the virus's ability to bind to and interact with the human angiotensin-converting enzyme 2 (ACE2) receptor. Some variants demonstrate heightened affinity for ACE2 receptors, potentially increasing the rate of virus transmission. (Alquraan et al., 2023). This study concentrated on the B.1.1.7 lineage, or Alpha variant, prevalent in the UK. This variant, distinguished by 17 mutations including N501Y, enhances viral attachment to host cells and demonstrates heightened transmissibility, estimated to be 43% to 82% greater than preexisting variants. Additionally, it is associated with increased disease severity and mortality rates compared to other strains. (Aleem et al., 2023).

1.2 Structural Characteristics of SARS-CoV-2

Coronaviruses are a type of enveloped viruses that possess a single-stranded RNA genome with a positive-sense, ranging from 26 to 32 kb in length (Roujian Lu et. al. ,2019). Within the Coronaviridae family, they belong to the Orthocoronavirinae subfamily. Among coronaviruses, SARS-CoV-2, the causative agent of COVID-19, is notable for having one of the largest RNA genomes, encoding a total of 29 proteins (Figure 1 a) (Yang et.al. 2021). Coronaviruses are further classified into four genera: α-, β-, γ-, and δ-coronaviruses. (Ahmad Abu Turab Naqvi et. al. 1866).

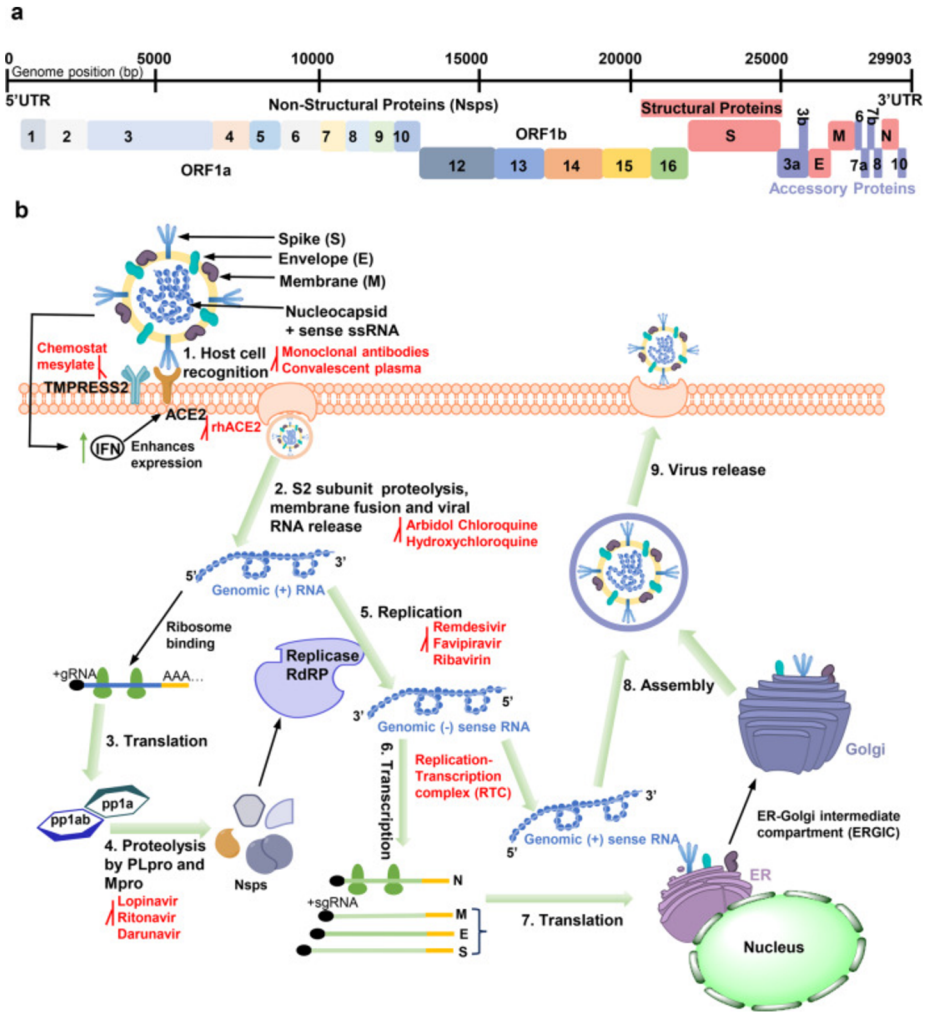

Figure 1: The whole genome composition and replication cycle of SARS-CoV-2 and potential targets. ***a*** *the viral genome encodes 16 nonstructural proteins.* ***b*** *the SARS-CoV-2 mainly infects lymphatic epithelial cells and type II pneumocytes with the initiation of human's body innate response by producing interferons (Yan W et. al., 2022) doi: 10.1038/s41392-022-00884-5*

SARS-CoV-2 is composed of four structural proteins, namely spike (S), membrane (M), envelope (E), and Nucleocapsid (N) proteins. Within the context of coronaviruses (CoVs), the spike (S) protein plays a pivotal role in attaching to the host cell-surface receptor during the process of host cell entry (Yu Lung Lau et. al., 2005). The S protein's interaction with the host receptor is mediated by the receptor-binding domain (RBD) located within the S1 subunit, followed by the fusion of the S2 subunit with the host cell membrane. In the context of virus-host interactions, it is important to note that distinct cell surface receptors are responsible for recognizing the receptor-binding domain (RBD) of spike (S) proteins in various coronaviruses, including SARS-CoV, MERS-CoV, and SARS-CoV-2. Specifically, MERS-CoV engages the dipeptidyl peptidase 4 receptor, while SARS-CoV and SARS-CoV-2 utilize the angiotensin- converting enzyme 2 (ACE2) receptor for binding to the viral S protein. (H. Zhang et. al. 2020; Kashwal et. al. 2022). In the respiratory tract, SARS-CoV-2 binds to angiotensin-converting enzyme 2 (ACE2) receptors primarily expressed on the surface of epithelial cells lining airways and alveoli, using its envelope-anchored spike protein to facilitate entry to host cells via endocytosis (Wan Y et al., 2020). The interaction between the virus and ACE2 receptors serves as a crucial step in viral entry, dictating its tropism and pathogenicity within the respiratory system. Once inside the host cells, viral replication ensues, leading to the formation of new virions (Figure. 1b). Subsequent release of these virions enables the virus to invade the neighbouring lung cells, causing cell death and triggering the initiation of immune responses. (Shereen et al., 2020; Boopathi et al., 2019). If the immune response fails to effectively control SARS-CoV-2 replication, massive lung injury occurs, triggering a hyperinflammatory 'cytokine storm' or the development of COVID-19 associated acute respiratory distress syndrome (ARDS), a potentially life-threatening complication (Li X et al., 2020; Coperchini et al., 2020). Notably, SARS-CoV-2 infection disrupts the pulmonary lining, which can lead to alteration in the normal microbiota of the respiratory tract, potentially predisposing individuals to secondary bacterial pneumonia (Handa et al., 2018). Moreover, the virus employs various evasion mechanisms to evade host immune responses, including double-membrane vesicle lacking pattern recognition receptors (PRRs), interference with interferon signaling through its surface proteins and mimicking host cell capping machinery (Li X et al.,2020; Totura et al.,2012). However, in the research using mice as model organisms, a caveat arises as mice do not possess human ACE2 receptors and SARS-CoV-2 cannot infect them. Therefore, mice must be modified with and expressing human ACE2 protein on their cells prior to the experiments (Gawish et al. 2022). The interaction between the spike (S) protein of SARS-CoV-2 and the angiotensin-converting enzyme 2 (ACE2) receptor is crucial for viral entry

into host cells. Understanding the role of ACE2 in viral entry provides valuable insights into the pathogenesis of COVID-19 and potential targets for therapeutic intervention. (Beyerstedt et al. 2021; Wan Y et al., 2020; Astuti et al., 2020, Chen et al., 2019).

1.3 Lung Structure and Function

1.3.1 Lung Anatomy and Alveolar Structure

The lungs, vital organs of respiration, are enveloped by a delicate double-layered serous membrane known as the pleura which serves to protect and cushion the lungs, secreting a small amount of fluid that acts as a lubricant, allowing the lungs to move smoothly in the chest cavity during breathing (Charalampidis et al. 2015). Their primary functional units, the alveoli, facilitate the exchange of gases. An adult human typically possesses around 300 million alveoli, collectively providing approximately 80 square meters of surface area for gas exchange (Deerinck et al., 2010; Khan YS et al., 2023).

1.3.2 Alveoli and Gas Exchange

A pulmonary alveolus, commonly referred to as an air sac, constitutes one among numerous empty spaces facilitating the exchange of oxygen and carbon dioxide between the lungs and the bloodstream during respiration. Inhaled oxygen traverses the alveoli into the bloodstream, circulating throughout the body, while carbon dioxide, originating from the body's tissues, traverses the blood and exits the body through exhalation after passing through the alveoli (Maina et al., 2005; Mous et al., 2018;). Type I pneumocytes (Figure 2, B), which constitute approximately 70% of the inner surface of each alveolus, possess a thin and flat structure, making them well-suited for gas exchange between the alveoli and the bloodstream. These cells exhibit extreme thinness, measuring as little as 25 nm and collaborate with the pulmonary capillary endothelium, to create the air-blood barrier, facilitating efficient gas exchange (Gray et al., 2021). Through tight junctions, these pneumocytes create a seal with neighboring cells, effectively restricting fluid infiltration into the alveoli. On the other hand, Type II pneumocytes (Figure 2, A) cover about 7% of the internal surface of each alveolus. These cells have a smaller volume compared to Type I pneumocytes and are characterized by apical microvilli. They contain lamellar bodies (Figure 2A- highlighted in yellow) within their cytoplasm, which store surfactant—a substance crucial for reducing the surface tension within the alveoli (Brandt JP et al., 2023; Patel et al., 2023; Terry et al., 2016).

1.3.3 Endothelial Cells and Vascular Function

Endothelial cells (ECs) (Figure 2, C) form the lining of small capillary blood vessels, facilitating the delivery of nutrients, oxygen, and cellular components to tissues while removing carbon dioxide and waste products. Beyond these essential functions, ECs play a crucial role in forming the vascular niche, where they interact with neighbouring cells such as epithelial, mesenchymal, and immune cells to regulate development, homeostasis, and regeneration in various organs. Through the secretion of angiocrine factors, ECs orchestrate these processes within the vascular niche. While well-characterized in organs like bone marrow and neurons, the impact of endothelial signals on other resident cells and the anatomy of the vascular niche in the lung remain underexplored. This review explores the role of alveolar capillary ECs in the vascular niche during development, homeostasis, and regeneration (Mammoto et al., 2019). Alveolar capillary endothelial cells are composed of two distinct cell types: aerocytes and general capillary cells (Schupp et al.,2021). Aerocytes, a subtype of endothelial cells are primarily confined to lung tissue and primarily facilitate gas exchange and leukocyte movement. A recent analysis conducted by Schupp et. al of endothelial cell profiles in both mouse and human lungs suggests a higher prevalence of aerocytes in human lung capillaries compared to mice. These specialized endothelial cells form a single-layered structure, in direct contact with the basement membrane, pneumocytes, and circulating blood cells, exhibiting specialized morphological and ultrastructural features conducive to their functions in gas exchange and immune cell trafficking (Comhair et al.,2012; Alberts B et al., 2002).

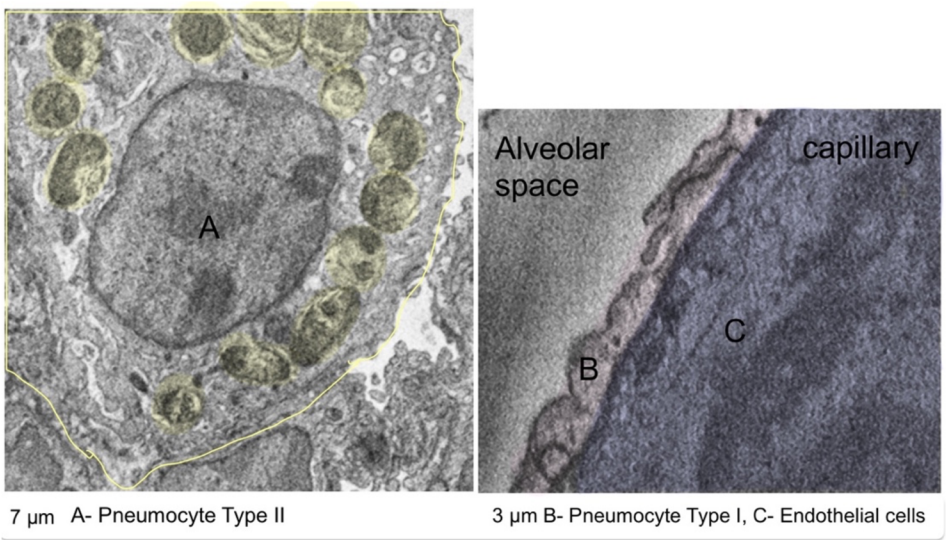

Figure 2: Pneumocyte Type II (left image, marked by A), Pneumocyte Type I (right image, marked by B) and Endothelial Cell (in right image marked by blue and C). Image from SBF-SEM dataset.

1.3.4 Thrombocytes and Immune Responses

Platelets or thrombocytes are the tiniest cells of the blood, typically measuring about 2 to 4 µm in diameter (Figure 3). They are anucleate, discoid cells and play a crucial role in stopping bleeding and preventing harmful blood clots (Thon JN et al., 2012). Recent studies indicate that they also detect infections and assist in inflammation. Furthermore, they link our body's basic and more complex immune responses, influencing both clotting and immune defense in the lungs. Despite their seemingly simple nature, platelets undergo changes in response to bodily cues (Elizabeth A. et al., 2016).

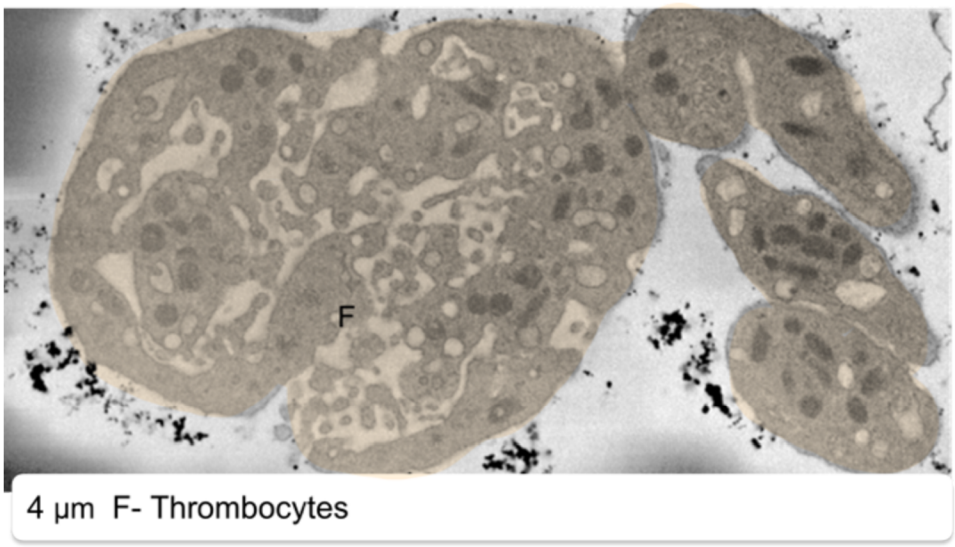

Figure 3: Thrombocytes (F) outside of the capillary. Image from SBF-SEM dataset

1.3.5 Erythrocytes

Erythrocytes, commonly known as red blood cells (RBCs), are the predominant blood cells responsible for transporting oxygen throughout the body's tissues (Figure 4). Evaluating the quantity of these vital cells often serves as the initial diagnostic measure in assessing a patient's overall health. RBCs lack a nucleus and adopt a distinctive biconcave disc shape, characterized by central pallor, known as discocytes. Their typical diameter ranges from 6 to 8 µm (Montoya-Navarrete et al., 2022). Hemoglobin, a complex molecule comprising proteins and iron, plays a pivotal role in oxygen transport. Within the lungs, hemoglobin binds to oxygen, forming oxyhemoglobin, which exhibits a bright red color. This oxygenated hemoglobin is then transported to body tissues, where it releases oxygen molecules, transforming into deoxyhemoglobin, also known as reduced hemoglobin, resulting in a darker red hue. The size, shape, and quantity of erythrocytes, as well as the hemoglobin count, significantly influence an individual's health status. Anemia, characterized by a deficiency in RBCs or hemoglobin, has widespread effects due to the reduced delivery of oxygen to tissues throughout the body (OpenStax CNX).

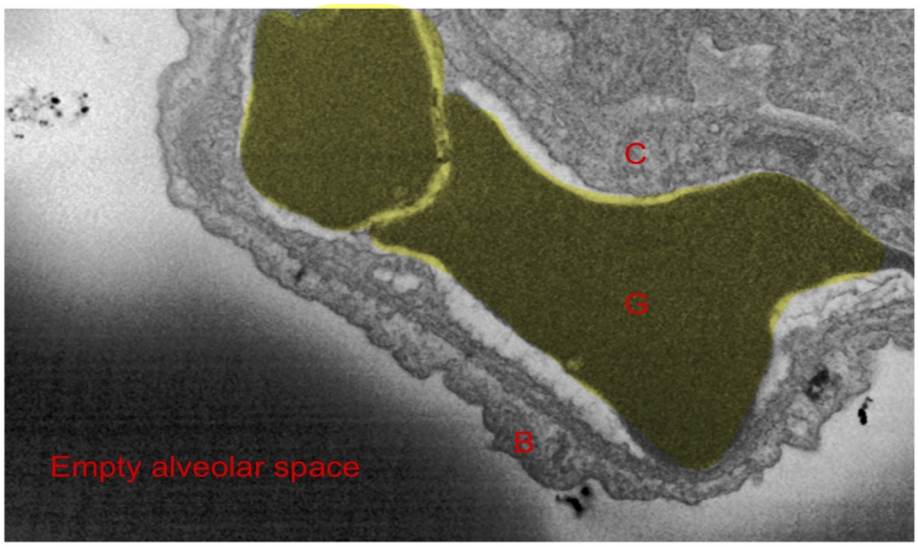

Figure 4: Erythrocyte (G) (Depicted in yellow); Image from SBF-SEM dataset

1.3.6 Alveolar Macrophages

As depicted in Figure 5, alveolar macrophages are the lung's primary defense against pollutants and pathogens and play a crucial role in initiating innate immune responses. They are located within the airways and at the alveolar level in the lungs, positioned away from the alveolar walls (Weinberger SE et al., 2019). When examined under an electron microscope, alveolar macrophages are easily identified by their distinctive morphology, characterized by irregularly shaped nuclei and abundant cytoplasm containing phagocytic vacuoles or engulfed particles. They typically have a larger size compared to surrounding cells within the alveolar space and are further distinguished by extensions resembling small “tentacles” around the cell, setting them apart from other cell types. Of particular importance are the lysosomes contained within these cells, which harbor digestive enzymes necessary for breaking down engulfed substances. (Naeem et al., 2022). These macrophages exhibit remarkable plasticity, with two distinct phenotypes identified: classically activated macrophages (M1) and alternatively activated macrophages (M2). M1 macrophages respond to microbial factors and proinflammatory cytokines, engaging in glycolytic metabolism and releasing inflammatory cytokines to enhance bacterial killing and recruit immune cells to the lung. In contrast, M2 macrophages, induced by anti-inflammatory signals, undergo oxidative metabolism, and contribute to inflammation resolution and tissue repair through efferocytosis and collagen deposition. Alveolar macrophages' diverse functions are dependent on their ontogeny and the lung's microenvironment, which influences their transcriptome and epigenetic landscape. These macrophages dynamically adapt to environmental cues, exhibiting various inflammatory phenotypes, and communicate extensively with other lung cells to regulate homeostasis and immunity. Despite challenges in distinguishing subpopulations, ongoing research aims to identify markers and profiles to understand their roles in lung health and pathology. Within the lung's intricate environment, alveolar macrophages interact with epithelial cells, microvascular endothelial cells, neutrophils, lymphocytes, fibroblasts, and stem cells, contributing to lung homeostasis and immunity (Brandt JP et al., 2023; Naeem A et al., 2022; Hu G et al., 2019).

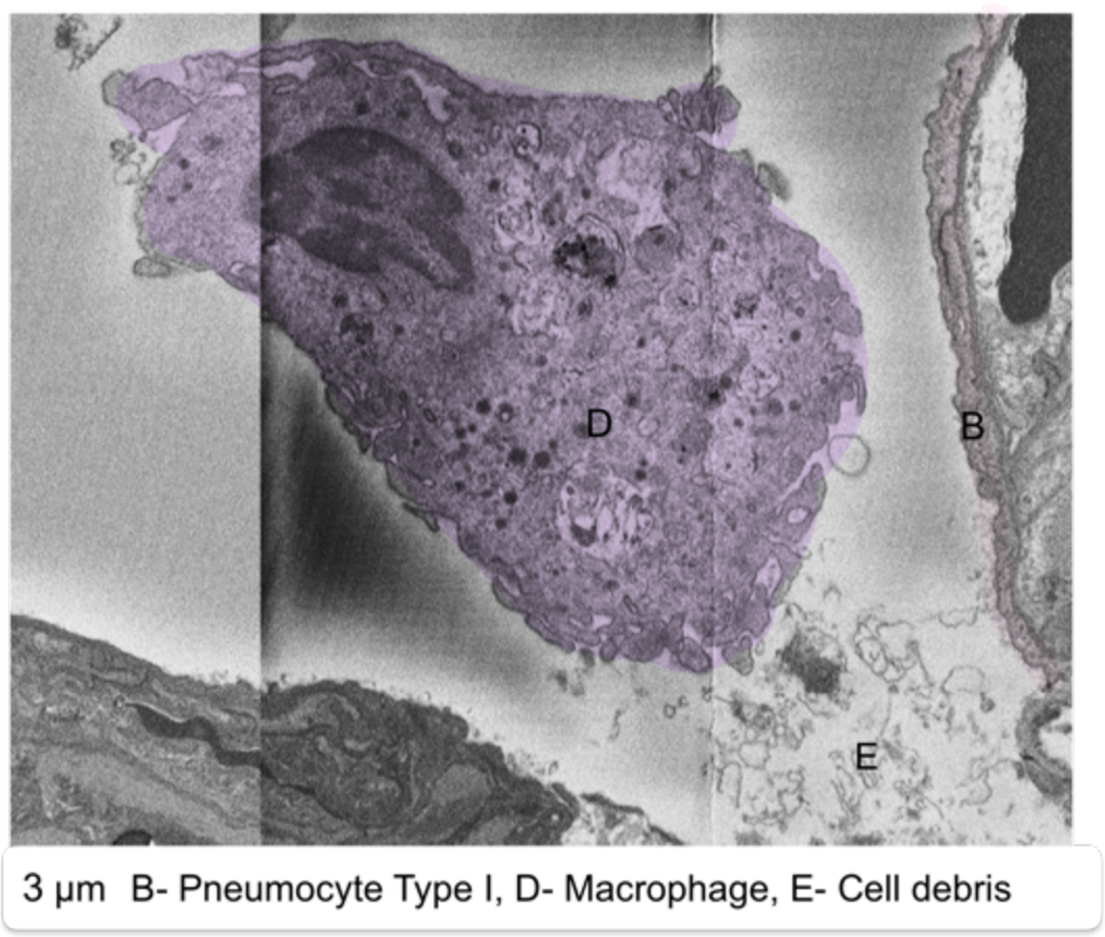

Figure 5: Depiction of a Macrophage (D) undergoing phagocytosis of (E) Cell debris.; Image from SBF-SEM dataset.

1.4 Lung immunity

The alveolar surface, being the largest area of the human body directly exposed to the external environment, serves also as a primary defense against invading microorganisms. A continuous layer of pulmonary epithelial cells acts as both a physical and biological barrier, reinforced by the mucus coating, proteolytic enzymes, and defense proteins like immunoglobulins, lactoferrin, and defensins. Pulmonary epithelial cells, equipped with pattern-recognition receptors like toll-like receptors (TLRs), closely interact with immune cells, secreting cytokines, and chemokines for immune response (Inverinzzi et al., 2020; Lloyd et all., 2017). Importantly, the lung houses immune cells such as dendritic cells, alveolar and interstitial macrophages, T-cells, γδ T-cells, NK cells, B-cells, innate lymphoid cells, and neutrophils, supporting innate and adaptive immunity (Nicod et al., 2005). Regulatory T cells maintain immune tolerance influenced by local microbiota, while lung resident memory γδ T cells provide rapid responses at barrier surfaces against previously encountered antigens. Despite these immune mechanisms, the potential for lung infections persists.

1.5 Serial block-face scanning electron microscopy

Volume EM imaging includes techniques such as Serial Block Face Scanning Electron Microscopy (SBF SEM) and Focused Ion Beam Scanning Electron Microscopy (FIB-SEM). Unlike traditional electron microscopy methods, volume SEM techniques have the unique capability of capturing serial images from a specimen, providing a three-dimensional view of the sample. SBF SEM, a prominent volume EM technique, involves capturing image data directly from the surface of a specimen within the chamber of a scanning electron microscope (SEM) (Haddad et al., 2023; Tapia et al., 2012). This process requires tissues to be pre-treated with heavy metals and embedded in epoxy resin before insertion into the SEM. The microscope is equipped with an ultramicrotome, a device capable of cutting very thin slices, housing a built-in diamond knife. After cutting a flat surface from the specimen block and retracting, the block undergoes scanning in a raster pattern with an electron beam, producing an image of the tissue's ultrastructure. The block is then elevated by a specific z-value, allowing for the cutting of a new surface. Repeating this sequence produces a stack of images from which 3D images can be reconstructed (Tapia et al., 2012). The signal generation for these images relies on backscattered electrons (BSE) generated when atoms are struck by an electron beam (Haddad et al., 2023). Staining with heavy metals increases the abundance of heavier atoms in the cellular structures. Therefore, heavy metal impregnation increases the BSE yield and increases both the conductivity and the contrast of the tissue (Tapia et al., 2012). SBF SEM can achieve a lateral resolution of approximately 5 nm^2 and a minimum slice thickness of about 25 nm for most biological systems. The total volume examined ranges from 1000 nm^3 to over 1,000,000 nm^3, allowing the study of various specimen types such as cells, tissues, organs, microorganisms, and synthetic materials. ROI size is big enough to visualize tens or even hundreds of cells and therefore imaging even bigger pieces of tissue is possible. This distinction is noteworthy as it aligns with the use of tissue samples in the study. Larger volumes can be attained by stitching together multiple overlapping images, expanding the observable area (Peddie et al., 2014, Courson et al., 2021).

1.6 Lung stereology

Stereology, tracing back to its inception in 1777, signifies a pivotal method for extracting 3D insights from 2D observations. Originating from Buffon's groundwork, this technique has revolutionized the understanding of complex structures like the lung (V.Brusaco et al., 2010). Stereology bridges the gap between flat slices and the true 3D nature of biological tissues, enabling the analysis of sectional profiles to reveal details about size, shape, volume, and orientation of structural components. Key principles like Cavalieri's Principle enable accurate volume estimation, while techniques such as planimetry and the fractionator facilitate parameter estimation. Modern stereological studies leverage computer-assisted tools and advanced equipment to ensure precision and reproducibility. In essence, stereology empowers researchers to unravel the intricate architecture of biological structures, offering valuable insights into their spatial organization and relationships. As a fundamental tool in scientific inquiry, stereology continues to drive advancements in various fields (Altunkaynak et all., 2012).

2 Work aim

- Understanding the changes and disease progression in mouse lung cells caused by SARS-CoV-2 infection.

3 Materials and Methods

3.1 Tissue Preparation for Electron Microscopy

Infectious virions of SARS-CoV-2 British Mutation were injected into genetically modified mice expressing the ACE2 protein, a receptor crucial for viral entry into cells (Li et all., 2003) Subsequently, lung tissue samples from infected mice were collected at two different time points (2 days post infection and 5 days post infection) for examination. The dissected lung tissues were promptly fixed and transported to the Laboratory of Electron Microscopy in České Budějovice for further analysis. Uninfected lung tissue samples from humanized mice (hACE2 transgenic mice) were also available for comparison, provided for EM analysis by M. Paulus, Ph.D., Laboratory of Arbovirology, Institute of Parasitology, Biological Center.

3.1.1 Chemical fixation

To prepare a sample for SBF-SEM, the lung tissue was fixed in a solution composed of 2,5% glutaraldehyde (SPI), 2% formaldehyde (Polysciences), and 150 mM sodium cacodylate (Sigma C5670) with a pH of 7,4, along with 2 mM calcium chloride. For the solution, 2 g of paraformaldehyde was dissolved in 40 ml of water heated to 65 °C, and approximately 10-20 µl of 10N sodium hydroxide were added for clarification. After cooling to room temperature, 50 ml of 0,3M sodium cacodylate with 4 mM calcium chloride (pH 7,4) was added, followed by the addition of 10 ml of 25% glutaraldehyde, and the pH was verified. A fixative solution volume of 50 ml per mouse lung infected was employed. The dissected tissue was cut into pieces smaller than 0,5 mm^3 using two scalpels, minimizing compression during the cutting process. The tissue sample was left to incubate and fix at room temperature for 6 hours and then stored in the fixative solution at 4 °C until further preparation for the electron microscopy sample.

3.1.2 Washing, Post fixation and Staining

The initial step involved washing the sample with 150 mM cacodylate buffer. The obtained tissue pieces were placed in glass bottles along with 10 ml of the prepared buffer, and the bottles were shaken on a shaker. In each interlude between rinsing cycles, the solution surrounding the sample tissue was replaced with 10 ml of fresh 150 mM cacodylate buffer, achievable through pouring or

aspiration. The washing solution was changed five times, three minutes at each step. The subsequent application of the osmium tetroxide-thiocarbohydrazide method, developed in 1960 by Hanker and Seligman, required the exchange of cacodylate buffer around the sample with a mixture of 4% osmium tetroxide (https://www.2spi.com/) and 3% potassium hexacyanoferrocyanide (II) trihydrate puriss (Sigma-Aldrich, 31254). Following this, a Thiocarbohydrazide (TCH) solution was prepared by combining an equal amount of 3% hexacyanoferrocyanide (II) trihydrate in 0,3M sodium cacodylate buffer with 4 mM calcium chloride and 4% osmium tetroxide in water. The sample underwent a 2-hour incubation at room temperature. To dispose of the cacodylate buffer, a specialized waste bottle (Polaron Equipment, 2402/6) was utilized. For a 3% potassium hexacyanoferrate (II) trihydrate solution, 0,3 g needed to be weighed in a 125 ml beaker and mixed with 10 ml of 0,3M cacodylate buffer. After stirring, the solution was used to wash the sample three times at room temperature with a 3-minute incubation period between each washing step. Next, a 1% TCH solution was created by mixing 0,1g of TCH (Sigma) with 10 ml of water, periodically stirring it for an hour after slight heating. After filtration, the sample was immersed in the solution for 1 hour. Post-incubation, the sample underwent five washes with double-distilled water for 3 minutes each. For the subsequent post-fixation step, a 2% osmium tetroxide solution was required, achieved by mixing the initial 4% solution in a 1:1 ratio with double-distilled water. The sample incubated in this solution for 30 minutes at room temperature, followed by five rinses with double-distilled water, each with a 3-minute incubation period between exchanges. After the washing step, a 1% uranyl acetate solution was prepared by dissolving 0,1g of uranyl acetate (EMS, 22400) in 10 ml of water, stirring for approximately 2 hours, and filtering three times over filter paper. The sample was then placed in the 1% uranyl acetate solution and stored in dark in the refrigerator at 4°C overnight. The following day, the sample underwent five additional washes with double-distilled water, with a 3-minute incubation period between each washing step. Subsequently, a Walton's lead aspartate solution was prepared by dissolving 0,998 g of L-aspartic acid (Serva, 14180) in 250 ml of double-distilled water, adjusting the pH to approximately 3,8, and adding 0,066 grams of lead nitrate (Analar R 672073). The solution was used to incubate the sample for 30 minutes in a laboratory oven at 60 °C. After cooling to room temperature over a 2-hour period, the sample underwent five washes, each involving a 3-minute incubation time with double-distilled water.

3.1.3 Dehydration

After completing the staining phase, dehydration was accomplished through a progressive series of acetone concentrations (30-50-70-80-90-95-100-100%). The sample underwent immersion successively in 10 ml of 30%, 50%, and 70% acetone solutions. At this juncture, the dehydration process could be halted, and the samples were stored at 4 °C overnight. During solution exchanges, the sample was placed on the shaker for 15 minutes at room temperature. To resume the process, the same steps were repeated using 10 ml of 80% acetone, followed by 90%, 95%, and finally, two rounds of 10 ml of 100% acetone solutions. In each interval between solution exchanges, the sample underwent 15 minutes of shaking at room temperature.

3.1.4 Resin Infiltration and Embedding

Following the dehydration process, the next step involved infiltration with Hard Plus Resin 812 (EMS, 14115) in a four-step procedure. Initially, the sample was immersed in a 25% mixture of resin from the Hard Plus Resin 812 kit and 75% acetone. Since this kit comes pre-mixed and pre-measured, the components are combined according to the manufacturer's instructions. Each kit contains five mini-kits, each capable of yielding approximately 100g of resin. The resin, prepared as per the manufacturer's guidelines, was stored in the freezer at -20°C using plastic syringes until needed. Before use, the defrosted resin-filled syringe could only be opened once it reached room temperature. For the infiltration process, the sample was submerged in the 1:3 resin-acetone mixture for 2 hours, a step that was repeated twice. Initially, a 1:1 mixture was employed, and subsequently, a 75% mixture of resin and 100% acetone solution was used. The incubation time for the 50% mixture was 2 hours, while for the 75% mixture, it was 3 hours at room temperature. Following this, the sample was stored in pure resin overnight on a shaker. The infiltration process was then concluded by replacing the resin once more with 100% fresh Hard Plus Resin 812 and incubating for 6 hours at room temperature.

3.1.5 Embedding and Curing

On the subsequent day, pure resin was poured into a flat mold. The sample was meticulously extracted from the bottle and delicately positioned into the mold. To identify each sample, a small, numbered paper was also inserted into the molds alongside the sample. Polymerization of the resin was initiated by placing the mold in an oven set at 62 °C for a duration of 48 hours.

3.2 Trimming and Mounting of the samples

After the resin had undergone polymerization, the small block containing the sample was precision-trimmed to dimensions of 400 µm × 400 µm × 400 µm using the Ultramicrotome Leica EM UC6. The microtome sectioning speed was set at 100 mm/s, and the section thickness was adjusted to 400 nm. The block was separated from the rest of the material using a razor blade, ensuring that the tissue was exposed on all six sides. The obtained block was affixed to 7 mm aluminum specimen stubs (Agar Scientific) using cyanoacrylate glue. Once the sample block was securely positioned, the connection between the stubs and the block was coated with conductive silver liquid (EMS) and left to dry overnight. Following this, the sample on the pin was further refined to a size of 200 µm × 200 µm × 200 µm using a glass knife. To enhance the sample's conductivity, the entire sample on the pin underwent gold sputter coating (Leica EM ACE200 vacuum coater) for 3 minutes under rotation to ensure a uniform coating. Before the actual imaging process, the top 10-20 µm of the block was removed using a glass knife. The trimming and mounting procedures for the samples were carried out by a technician from the Laboratory of Electron Microscope.

3.3 Data Acquisition

The data collection process was conducted by Dr. Jiří Týč using the SBF-SEM Apreo microscope from Thermo Fisher Scientific. Three different data sets were obtained. Healthy mice lungs, 2 days post infection and 5 days post infection.

Table 1: Microscope Settings

Region of interest	ROI 1, ROI 2	ROI 1 B
Voltage	3,5 kV	3,5 kV
WD	8 mm	8 mm
Current	81 pA	81 pA
Pressure	30 Pa	30 Pa
Pixel size	7 nm	7 nm
Dwell time	3 µm	3 µs
Electron dose	19,1 e/nm^2	31 e/nm^2
Slice thickness	200 nm	200 nm

3.4 Processing and analysing data through the utilization of Microscopy Image Browse (MIB)

The analysis employed the open-access software Microscopy Image Browser (MIB), developed by I. Belevich et al. at the University of Helsinki (http://mib.helsinki.fi). This software facilitates the visualization, editing, and segmentation of light- and electron-microscopy image datasets with high performance (Belevich et al., 2016). Particularly beneficial for this experiment, the software supports multidimensional image processing (3D). Given the substantial size of the datasets involved, a robust PC with 128 GB RAM, available in the Laboratory of Electron Microscopy, was essential to ensure smooth operation throughout the entire data evaluation process.

3.4.1 Stereology

The quantification was conducted by using stereological methods, which provide a systematic approach for deriving information about the volume and number of structural components within three-dimensional (3D) structures. Stereological analysis began as shown in Figure 6, by establishing the grid over the tissue sample, with each intersection point serving as a sampling site. I determined what lies beneath each cross-section point of the grid and labelled/saved the point in the model file of MIB. I ended up with distinct categories for each structural elements present within the dataset. The following were identified and counted: pleura, lipofibroblast, endothelial cells (both damaged and healthy), capillary lumen, pneumocyte type 1 and type 2 (both damaged and healthy), immune cells (uncharacterized), macrophages, neutrophils, thrombocytes, granulocytes, erythrocyte, collagen fibers, uncharacterized necrotic cells, empty alveolar space. This meticulous process was repeated for each dataset across different slices, ensuring comprehensive coverage of the tissue sample. The grid spacing was defined in both XY (2 µm) and Z (5 µm) dimensions, to ensure to capture of even the smallest cells (thrombocytes) in our dataset. Specifically, the negative lung dataset had dimensions of 70 x 70 µm and consisted of 318 slices per 50 nm, the 2nd day post-infection dataset had dimensions of 148 x 75 µm and comprised 119 slices of 200 nm and the 5th day post-infection dataset had 158 x 158 µm and 157 slices of 200 nm. Upon completion of the analysis, a tally of counted points was generated for each cellular components, for every slice and dataset examined. This enabled the extrapolation of volumes from the datasets.

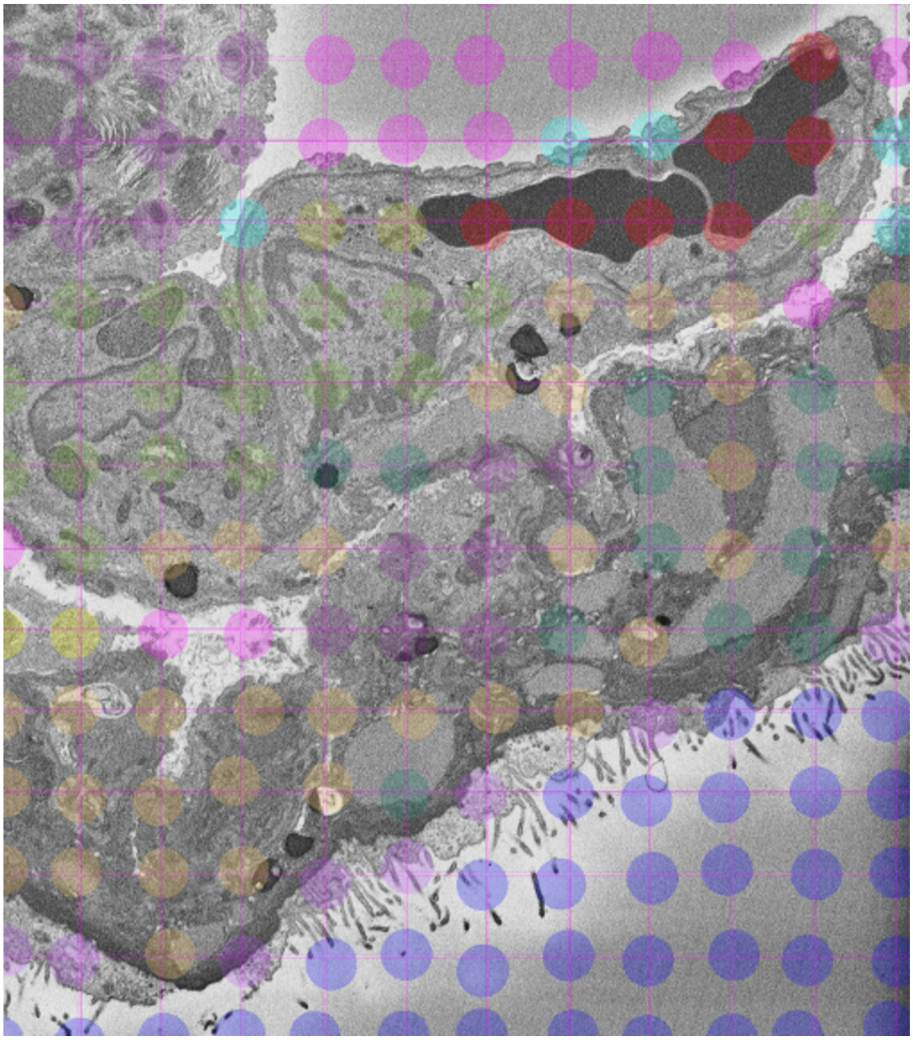

Figure 6: Snapshot of a tissue sample overlaid with a grid for stereological analysis. Various elements, including pleura are marked within the grid. This method allows for systematic sampling and identification of cell types in the sample, contributing to a detailed analysis of tissue composition and structure. (Purple: pneumocytes type II, blue: pneumocytes type I, green: endothelial cells, dark green: collagen fibers, orange: muscle fiber, red: erythrocytes, yellow: macrophage, dark purple: extracellular matrix, pink: alveolar space)

4) Results

In this chapter, I will summarize the findings from our investigation into the lung tissue during the COVID-19 disease caused by British mutation of SARS CoV-2. I will begin by comparing the values I have obtained among the negative lung control (representing healthy lung cells), values obtained from the second day post-infection and those obtained on the fifth day post infection.

4.1. Overall Overview of Dominant Elements

Table 2: Comparison of statistical values calculated in percent [%] of lung cell types in three different time slots (negative lung control, second day post-infection and fifth day post-infection)

Components	Negative lung control	Second day post-infection	Fifth day post-infection
Pneumocytes 2	2,99%	6,22%	6,60%
Pneumocytes 1	7,86%	2,65%	6,40%
Endothelial Cells	11,45%	8,51%	9,20%
Damaged Endothelial Cells	0,34%	1,51%	0,10%
Lipofibroblasts	8,57%	15,88%	6,80%
Macrophages	0,00%	2,41%	1%
Immune Cells	0,20%	0,16%	0,70%
Erythrocytes	3,81%	2,08%	2,50%
Necrotic Cells	0,14%	0,43%	0,80%
Empty Alveolar Space	51%	43,11%	57,60%
Thrombocytes	0,03%	0,03%	0,40%
Collagen fibers	1,25%	1,70%	2%

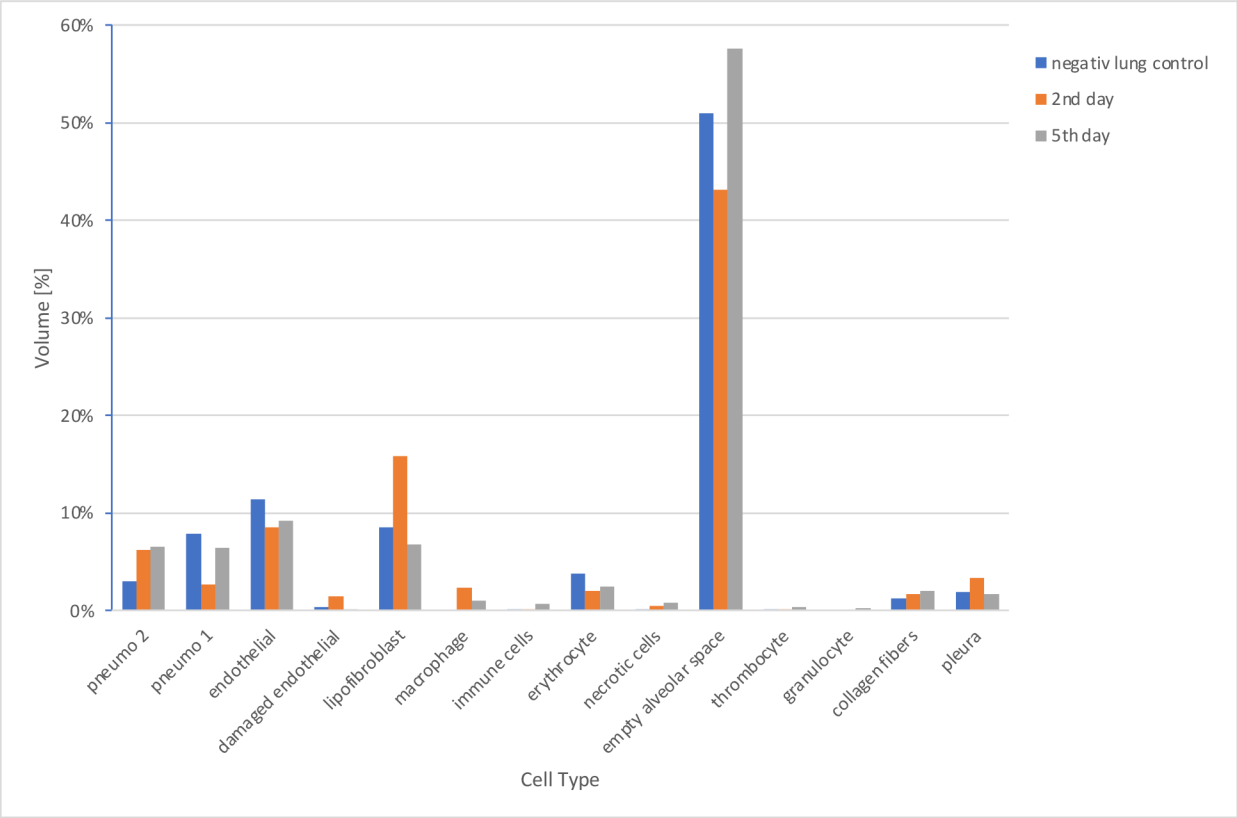

Graph 1: Comparison of statistical values of dominant elements calculated in volume %.

4.1.1 Overview of healthy lung cells:

Figure 7 captures a healthy mouse lung, revealing key cellular components. Macrophages are notably absent, indicating no acute infection or inflammation. Minimal necrotic cells suggest little cellular damage. Erythrocytes are plentiful, signifying efficient oxygen transport. Few lipofibroblasts are observed, contributing to lung structure. Overall, the image portrays the balanced functionality of healthy lung tissue.

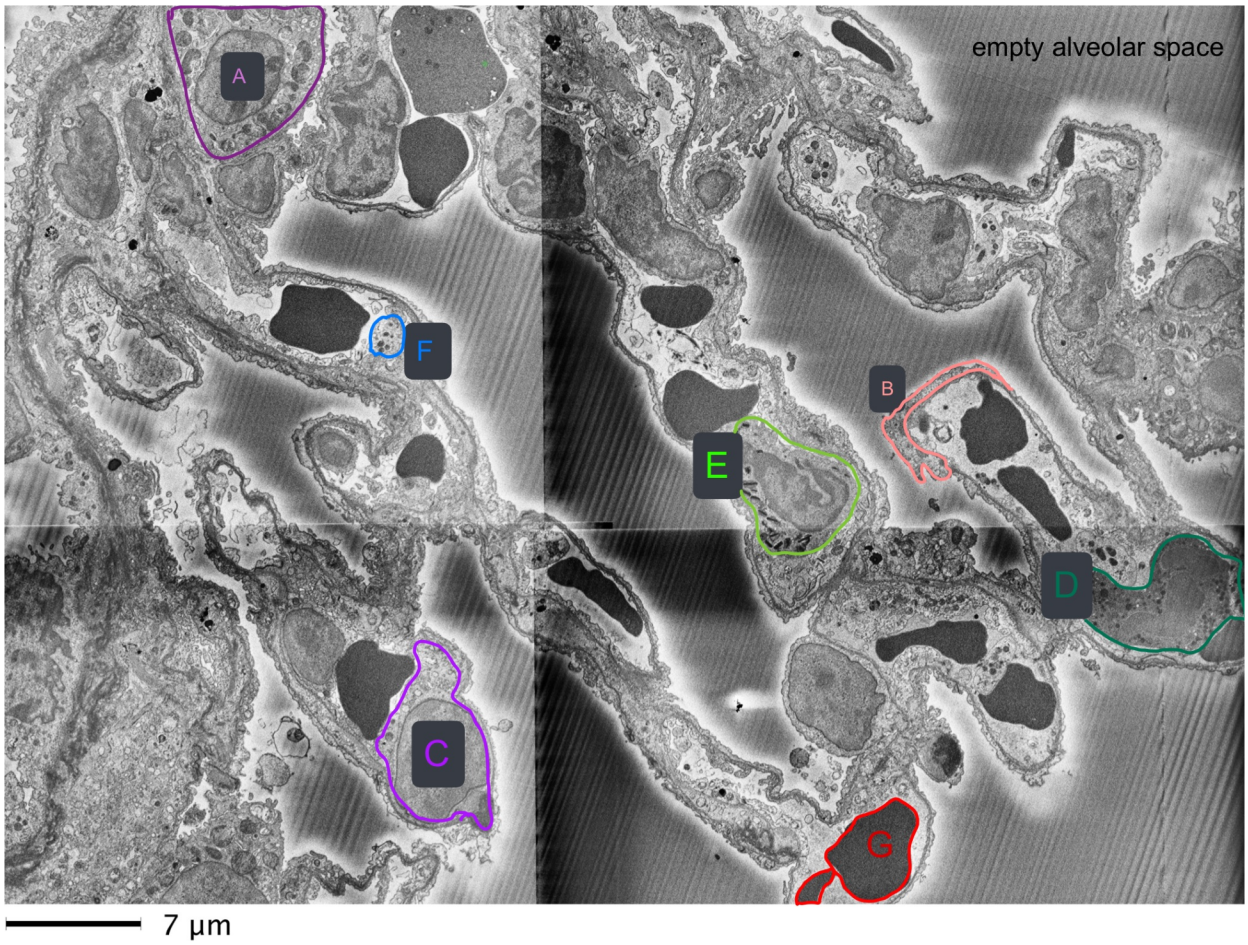

Figure 7: Overview of the healthy mice lung cells (A (dark purple)- Pneumocyte Type II, B (pink)- pneumocyte type I, C (purple)-endothelial cells, D (dark green) neutrophile, E (bright green) eosinophil, F (blue) thrombocyte, G (red)-erythrocytes)

4.1.2 Overview of second day post infection

On the second day post-infection, the lung tissue exhibits noticeable changes. Macrophages become visible. Additionally, there is an increase in necrotic areas (Figure 8, C). Moreover, collagen fibers appear more abundant in the infected lung by 1,7% in the second day compared to the negative control where we had 1,25%. (Figure 8, D). Furthermore, an increase in lipofibroblasts is observed from 8,57% in the negative lung control to 15,88% by second day post infection.

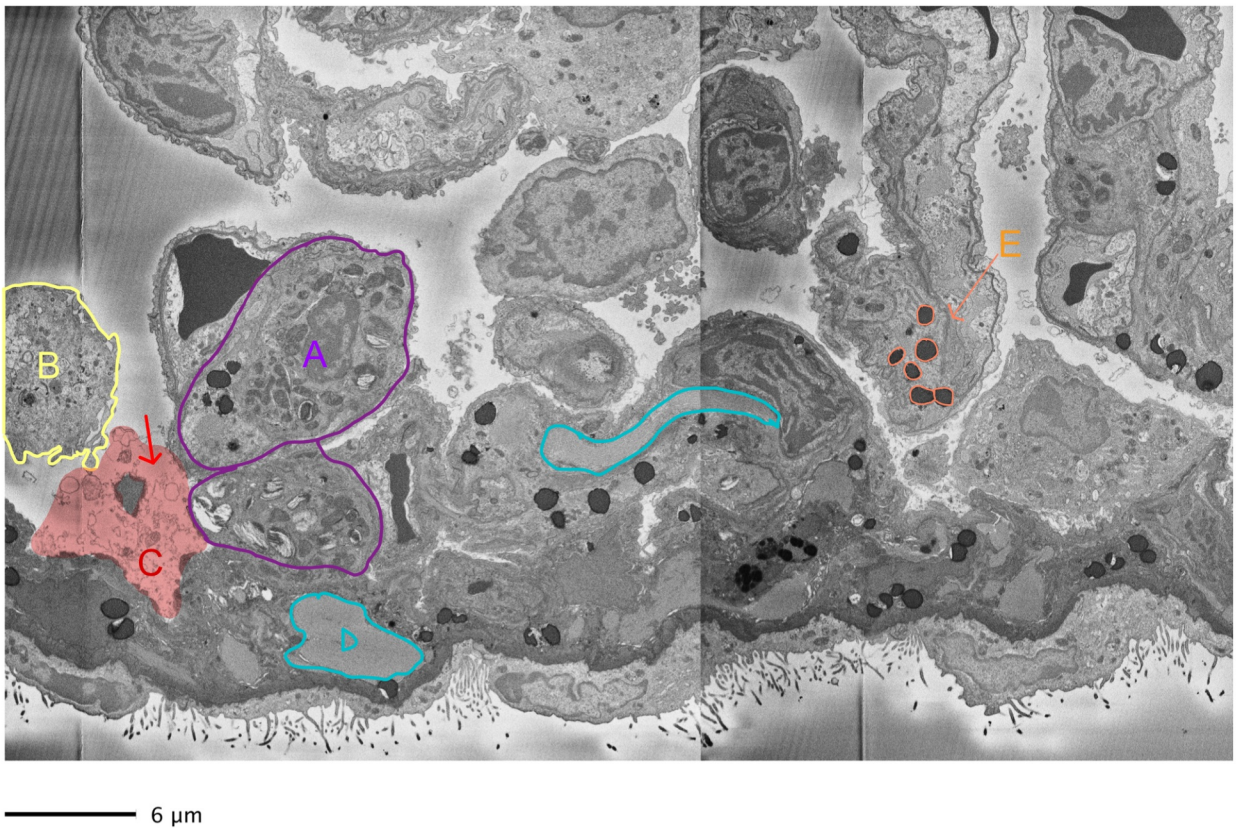

Figure 8: Overview of 2nd day post infection mice lung cells. (A- (dark purple) Pneumocytes Type II, B (yellow) macrophage going into C- necrotic area (red marked). D (marked in blue) collagen fibers and E represent lipofibroblasts marked in orange.

4.1.3 Overview of fifth day post infection

On the fifth day post-infection, further alterations are evident in the lung tissue (Figure 9). Macrophages are prominently visible. Moreover, there is a notable increase in cell debris compared to the second day. Additionally, there appears to be more empty space within the tissue, possibly reflecting areas where the cells have died off or where cell debris has accumulated.

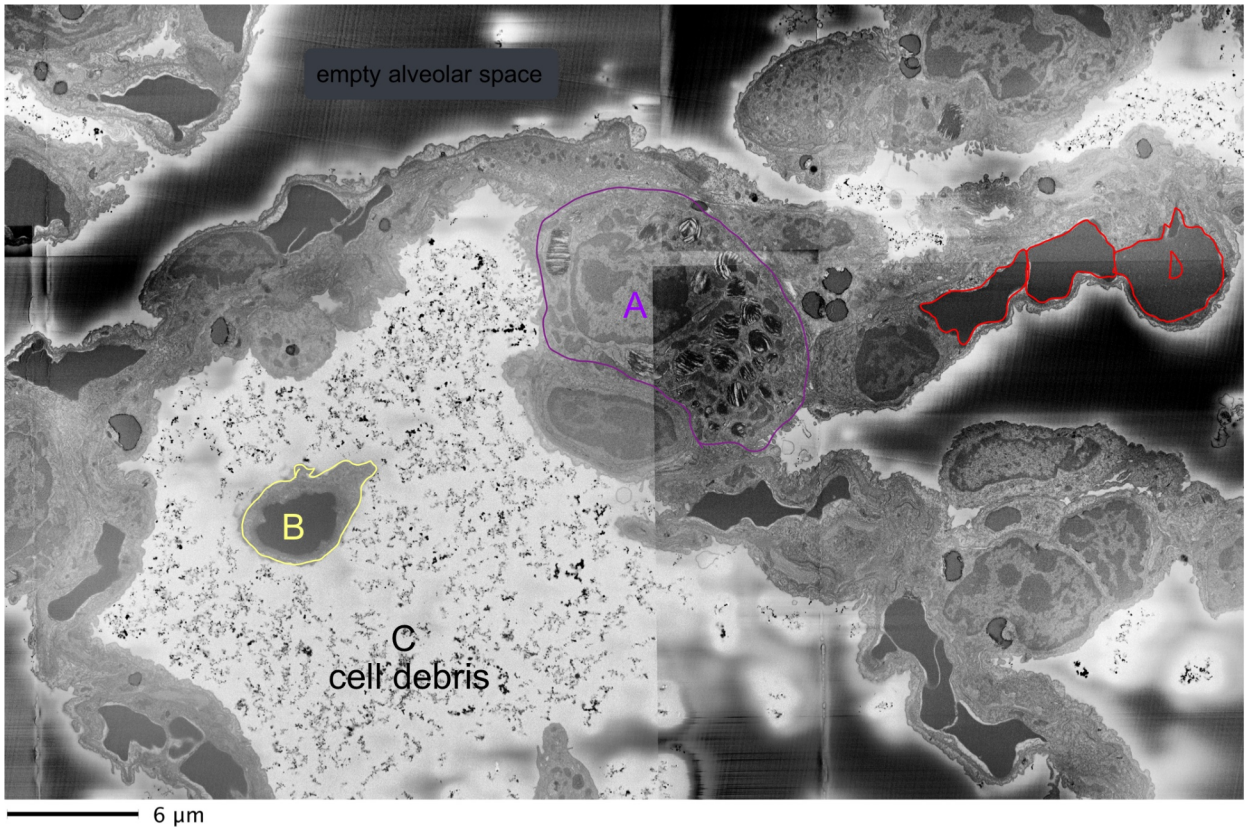

Figure 9: Overview of 5th day post infection mice lung cells (A- Pneumocyte Type II (marked in purple),B- Macrophage (marked yellow), C- the patterned area is cell debris and D- Erythrocytes (marked in red))

4.2 Increase of thrombocytes

Thrombocytes (Figure 11, marked in red) play a crucial role in clotting and can respond to infections and inflammation, linking the immune system with clotting processes and influencing lung health (Middleton et al., 2016). In both, negative lung control and second day post infection, thrombocytes were present at a level of 0,03%. However, in 5th day post-infection, there was a notable increase observed, up by 0,37%. Additionally, an intriguing observation is the presence of thrombocytes freely within the alveolar space (Figure 10).

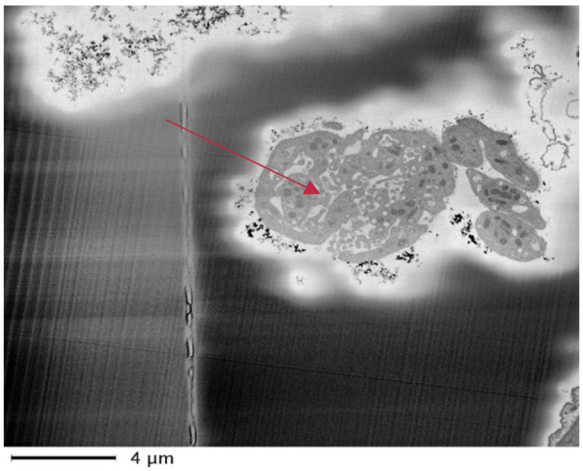

Figure 10: Thrombocytes found freely in the alveolar space, 5th day post infection. (arrow)

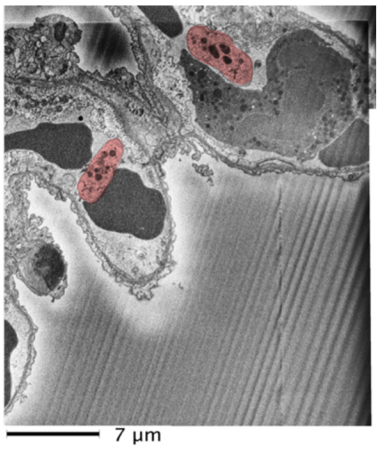

Figure 11: Thrombocytes (marked in red) found in vessel, capillary in negative lung control)

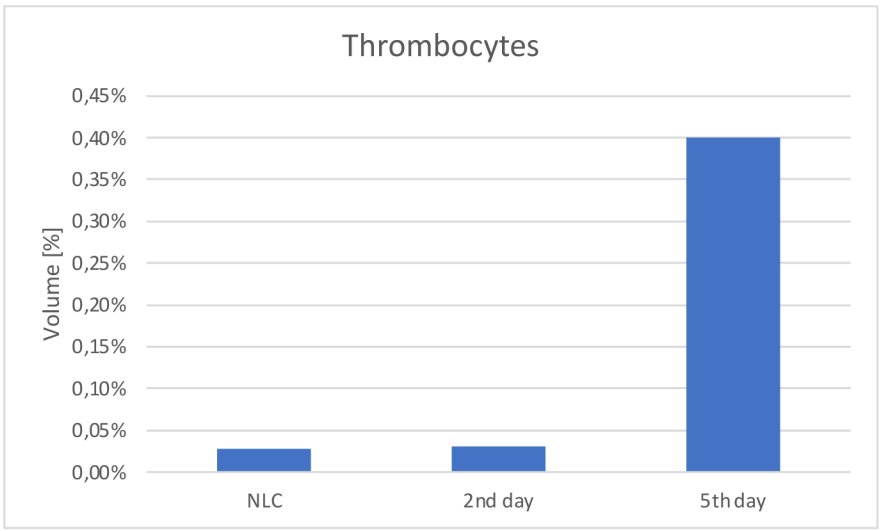

Graph 2: Thrombocytes increase in the negative lung control (NCL), second day post infection and fifth day post infection calculated in Volume %.

4.3 Increase of necrotic cells

In Figure 12, the presence of cell debris complicated the identification of cells undergoing necrosis. Figure 13 illustrates tissue damage and highlights necrotic cells in pink. Additionally, Figure 14 depicts endothelial cells undergoing necrosis. As shown in Graph 3, the prevalence of necrotic cells escalates with each passing day. In the negative lung control, necrotic cells accounted for only 0,14%, increasing to 0,43% on the second day, and nearly doubling to 0,80% by the fifth day.

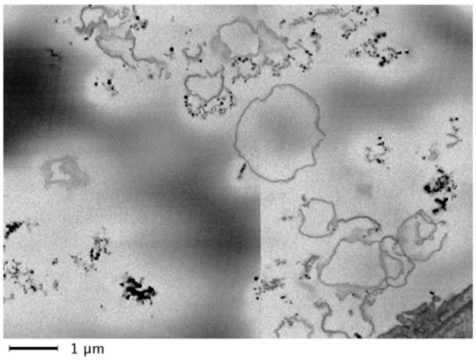

Figure 12: cell debris.

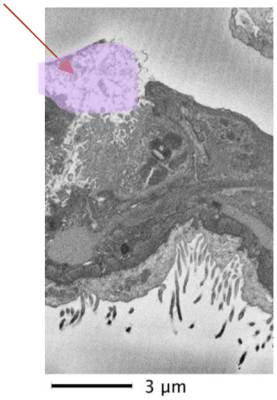

Figure 13: Necrotic cells (highlighted in pink) found in 5th day post infection.

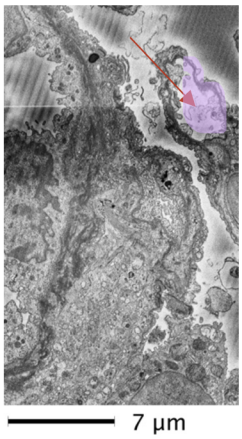

Figure 14: endothelial cells (highlighted din pink) undergoing necrosis.

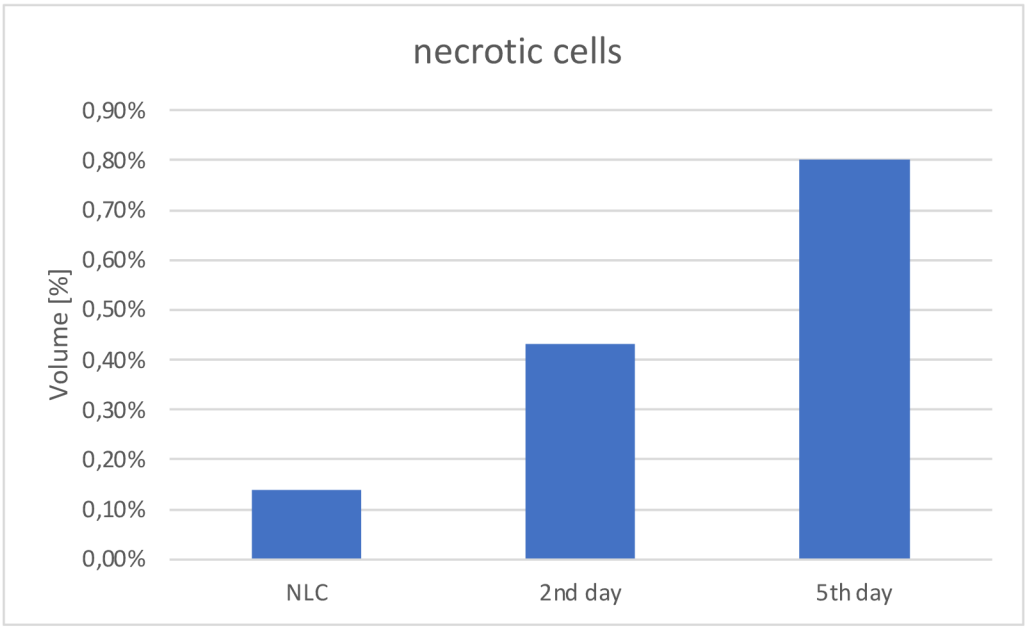

Graph 3: Necrotic cells representation in NCL, 2nd day post infection and 5th day post infection calculated in %.

4.4 Macrophages

During of the infection infection, the body recruits macrophages to the infected area as part of its defense mechanism against the virus. Macrophages were absent in the healthy lung state and first detected at 2,41% on the 2nd day post infection indicating an early immune response. However, by the 5th day post infection, macrophages presence decreased to 1%. Macrophages were often seen close to the cell debris or necrotic cells (Figure 15, Figure 16)

As shown in the Figure 15 and 16, a macrophage interacting with a cell debris (indicated by the red arrow) signifies event in the immune response.

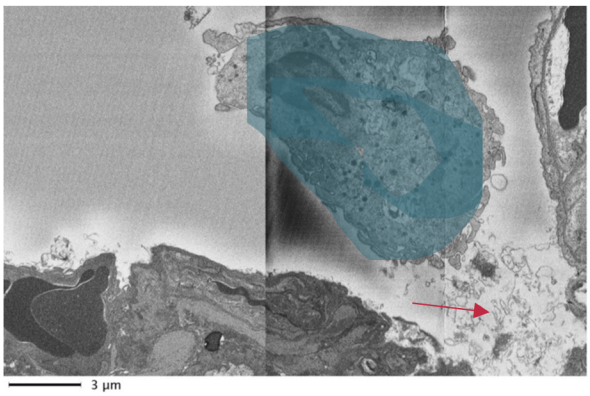

Figure 15: Macrophage (highlighted in blue), found near cell debris (indicated by the red arrow).

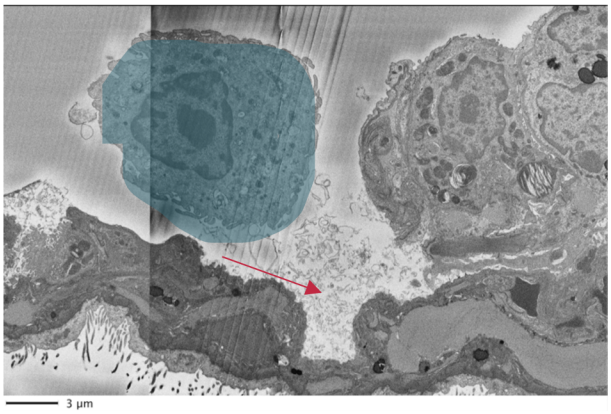

Figure 16: Macrophage (highlighted in blue) found near cell debris (indicated by the red arrow).

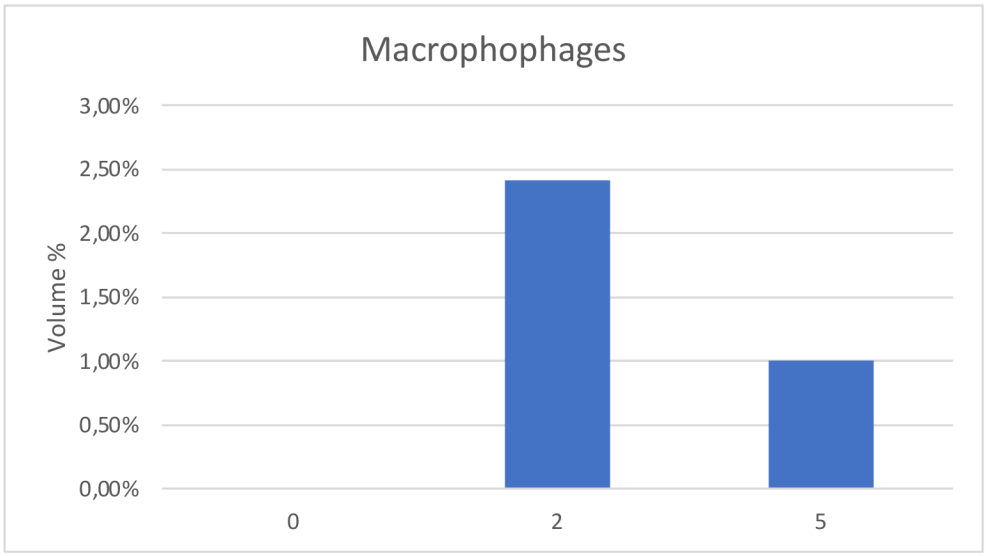

Graph 4: Macrophages increase at time: 0 (negative lung control), 2(2nd day post infection) and 5 (5th day post infection) calculated in Volume %.

4.5 Pneumocytes type I and II

Pneumocytes type II (Figure 17) are responsible for maintaining alveolar stability by secreting surfactant. In the negative lung control, they constitute almost 3%. On the 2nd day post-infection this rises to 6,22% and by the 5th day it increases further to 6,6%. However, there is a notable decrease of in pneumocyte type I cells (Figure 18) observed from the healthy lung state, where they constitute 7,86%, to the 2nd day post infection they drop to 2,65% and rising to 6,40% by the 5th day (Graph 5).

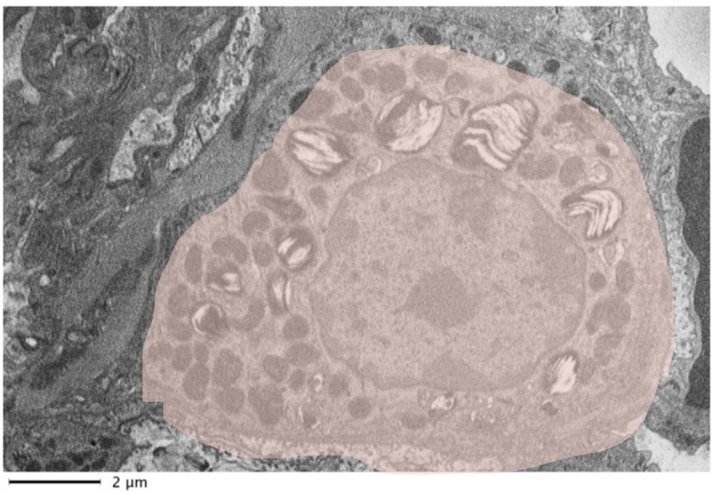

Figure 17: Depiction of a pneumocyte type II (highlighted in beige).

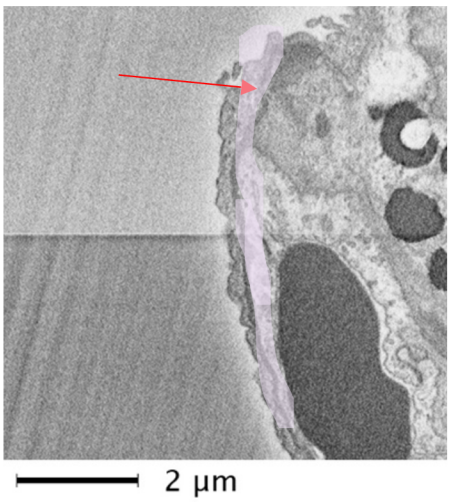

Figure 18: pneumocytes type I, highlighted in purple.

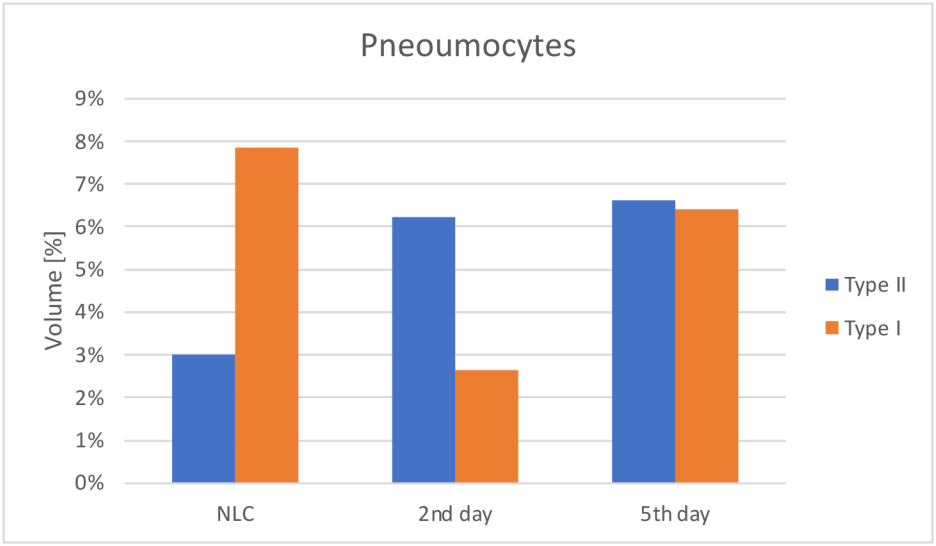

Graph 5: Pneumocytes type I (shown in orange) and pneumocyte type II (shown in blue), and those statistical values calculated in % of NGL (negative lung control), second day post infection and fifth day post infection.

4.6 Decrease of endothelial cells:

A decrease in endothelial cells is observed as early as the 2nd day post-infection, with no further decrease noted by the 5th day: 11,45% in the negative lung control, 8,51% on the 2nd day and 9,20% on the 5th day.

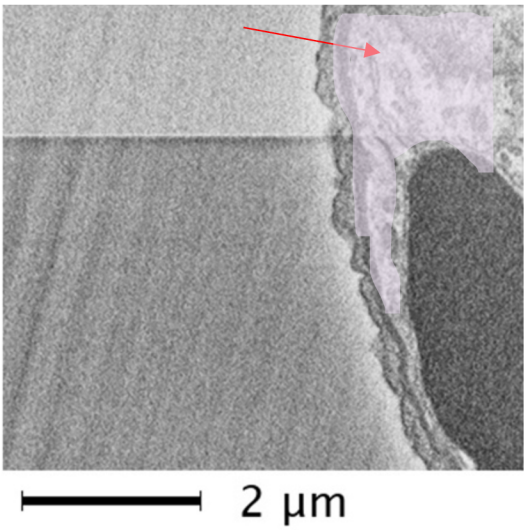

Figure 19: Depiction of endothelial cells, highlighted in pink.

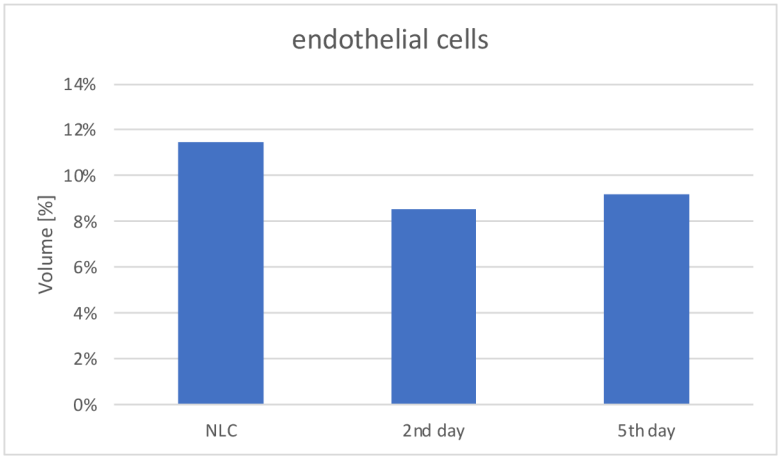

Graph 6: Statistical values of endothelial cells in NLC (negative lung control) 2nd day post infection and 5th day post infection.

5 Conclusion and Discussion

In the healthy lung cells, as depicted in Figure 7, a balanced functionality of the lung tissue is evident, characterized by the presence of essential cellular components such as erythrocytes for oxygen transport and minimal necrotic cells indicating little cellular damage. This serves as a baseline for comparison against infected conditions. Upon infection, particularly on the second day post-infection, notable changes emerge: an increase in pneumocyte type II cells from 2,99% to 6,22%, a decrease in pneumocyte type I cells from 7,86 to 2,65%, and the appearance of macrophages at 2,41%, an indicative of an immune response, along with increased necrotic areas, collagen fibers, and lipofibroblasts. These changes signify an initial tissue response to infection, including immune activation and tissue injury. As the infection progresses to the fifth day post-infection, further alterations in lung tissue are apparent, including a decrease in macrophage presence to 1%, an increase in lipofibroblasts from 8,57 to 15,55%, and an increase in necrotic cells from 0,43% to 0,80%. Those changes indicate an ongoing immune response, while the increasing presence of necrotic cells suggests continued tissue damage or progression of infection. Additionally, the presence of empty spaces within the tissue could suggests cell death or loss of tissue integrity, which are being prominent outcomes of infection and disease progression. Furthermore, the observed increase in thrombocytes, observed notably on the fifth day post-infection (Graph 2), presents an intriguing finding. Thrombocytes are known to play crucial roles in clotting, inflammation, and tissue repair. (Middleton et al., 2016). While elevated levels can potentially lead to thrombotic complications, potentially exacerbating the severity of the infection, we did not observe thrombosis in our study. However, the presence of thrombocytes within the alveolar space, as depicted in Figure 7, suggests that they may have formed clots and subsequently contributed to capillary rupture, releasing them into the alveolar space.

Regulated necrosis, a genetically programmed process, includes pathways like necroptosis and pyroptosis, influencing immune responses and tissue health. In COVID-19, these processes contribute to severe complications. Studying them offers insights into potential treatments (Sun C. et al., 2022). Necrotic areas suggest tissue damage due to infection, collagen fibers indicating a response to tissue injury, and lipofibroblasts should contribute to the repair process or inflammation. The observed changes in necrotic cell levels underscore the importance of studying regulated necrosis processes in COVID-19, as they influence immune responses and tissue health, potentially contributing to severe complications. Alveolar macrophages are vital for our immune system,

capturing inhaled particles and microbes like viruses and bacteria. They engulf pathogens and release inflammatory signals, enhancing the local immune response. Inside the macrophages, pathogens are destroyed through fusion with lysosomes (Brandt et al., 2023; Naeem et al., 2022). The detection of macrophages on both the second- and fifth-days post-infection suggests ongoing immune response during different stages of infection. The decline in macrophage presence on the fifth day post-infection may indicate effective pathogen clearance or changes in immune cell priorities. Furthermore, the increase in pneumocyte type II, responsible for maintaining alveolar stability, and the decrease in pneumocyte type I, potentially associated with the increase in necrotic cells, highlight the cellular dynamics involved in maintaining lung function during infection. Alveolar capillary endothelial cells are key players in maintaining tissue integrity and facilitating gas exchange (Mammoto et al., 2019). The early decrease in alveolar capillary endothelial cells, followed by a stable trend, suggests an early impact on tissue integrity, which may stabilize as the infection progresses. Based on the observed fluctuations between the 2nd and 5th days post-infection, it suggests potential complexity in the dynamics of cellular changes in response to infection. Speculatively, these fluctuations could arise from variations across different regions of interest (ROIs) in the lungs, each undergoing distinct stages of the infection evolution. For instance, the presence of lipofibroblasts on second day post infection may correspond with early-stage infection, while their absence on 5^{th} day could indicate a shift in cellular populations as the disease progresses. The transition from a healthy state to infected reveals alterations in lung tissue composition and cellular populations (see Table 2 for details). This underscores the importance for further investigation to elucidate the underlaying mechanisms driving these observed variations.

In conclusion, the investigation into the lung tissue to infection offers preliminary insights into the host-pathogen interaction during the early stages of infection. While the findings suggest potential trends in tissue response, it is important to acknowledge the limitations of the study, including lack of statistical significance and dynamic data. Further research with larger datasets and more comprehensive analysis would be needed to draw definitive conclusions. The observed fluctuations in cellular composition and dynamics underscore the complexity of the immune response and tissue damage mechanisms associated with infection progression. While the study identifies potential trends, such as recruitment of immune cells such as macrophages, increases necrotic cells, and changes in thrombocyte levels, it is important to note the preliminary nature of these findings. To enhance the study's findings, further examination of additional regions of interest is necessary.

Comparative analysis with datasets generated by other researchers could provide validation and contribute to a broader understanding of infection evolution. Moreover, exploring the underlying mechanisms driving these fluctuations, such as variations in immune response or pathogen kinetics, could offer deeper insights into disease pathogenesis and potential therapeutic targets.

6 References:

- Ahmad Abu Turab Naqvi, Kisa Fatima, Taj Mohammad, Urooj Fatima, Indrakant K. Singh, Archana Singh, Shaikh Muhammad Atif, Gururao Hariprasad, Gulam Mustafa Hasan, Md. Imtaiyaz Hassan, Insights into SARS-CoV-2 genome, structure, evolution, pathogenesis and therapies: Structural genomics approach, Biochimica et Biophysica Acta (BBA) - Molecular Basis of Disease,Volume 1866, Issue 10,2020,165878,ISSN 09254439,https://doi.org/10.1016/j.bbadis.2020.165878.(https://www.sciencedirect.com/science/article/pii/S092544392030226X)
- Alberts B, Johnson A, Lewis J, et al. Molecular Biology of the Cell. 4th edition. New York: Garland Science; 2002. Blood Vessels and Endothelial Cells. Available from: https://www.ncbi.nlm.nih.gov/books/NBK26848/
- Aleem A, Akbar Samad AB, Vaqar S. Emerging Variants of SARS-CoV-2 and Novel Therapeutics Against Coronavirus (COVID-19). 2023 May 8. In: StatPearls [Internet]. Treasure Island (FL): StatPearls Publishing; 2024 Jan–. PMID: 34033342.
- Altunkaynak, Önger , et all, A brief Introduction to Stereology and Sampling Strategies: Basic Concepts of Stereology, March 2012, DOI:10.14704/nq.2012.10.1.427
- Alquraan L, Alzoubi KH, Rababa'h SY. Mutations of SARS-CoV-2 and their impact on disease diagnosis and severity. Inform Med Unlocked. 2023;39:101256. doi: 10.1016/j.imu.2023.101256. Epub 2023 Apr 25. PMID: 37131549; PMCID: PMC10127666.
- Anatomy & Physiology. Provided by: OpenStax CNX. Located at: https://courses.lumenlearning.com/suny-ap2/chapter/erythrocytes/, retrieved: 12.04.2024.
- Astuti I., Ysrafil. Severe acute respiratory syndrome coronavirus 2 (SARS-CoV-2): an overview of viral structure and host response. *Diabetes Metab Syndrome: Clin Res Rev.* 2020;14(4):407–412.
- Beyerstedt S, Casaro EB, Rangel ÉB. COVID-19: angiotensin-converting enzyme 2 (ACE2) expression and tissue susceptibility to SARS-CoV-2 infection. Eur J Clin Microbiol Infect Dis. 2021 May;40(5):905-919. doi: 10.1007/s10096-020-04138-6. Epub 2021 Jan 3. PMID: 33389262; PMCID: PMC7778857.

- Boopathi S., Poma A.B., Novel K.P. coronavirus structure, mechanism of action, antiviral drug promises and rule out against its treatment. *J Biomol Struct Dyn.* 2019;2020:1–10.
- Brandt JP, Mandiga P. Histology, Alveolar Cells. [Updated 2023 Aug 28]. In: StatPearls [Internet]. Treasure Island (FL): StatPearls Publishing; 2024 Jan-. Available from: https://www.ncbi.nlm.nih.gov/books/NBK557542/
- Charalampidis C, Youroukou A, Lazaridis G, et al. Pleura space anatomy. J Thorac Dis. 2015;7(Suppl 1):S27–S32. doi:10.3978/j.issn.2072-1439.2015.01.48
- Chen N., Zhou M., Dong X., Qu J., Gong F., Han Y., et al. Epidemiological and clinical characteristics of 99 cases of 2019 novel coronavirus pneumonia in Wuhan, China: a descriptive study. *Lancet.* 2020;395(10223):507–513.
- Comhair SA, Xu W, Mavrakis L, Aldred MA, Asosingh K, Erzurum SC. Human primary lung endothelial cells in culture. Am J Respir Cell Mol Biol. 2012 Jun;46(6):723-30. doi: 10.1165/rcmb.2011-0416TE. Epub 2012 Mar 15. PMID: 22427538; PMCID: PMC3380284.
- Coperchini F., Chiovato L., Croce L., Magri F., Rotondi M. The Cytokine storm in COVID-19: An overview of the involvement of the chemokine/chemokine-receptor system. *Cytokine Growth Factor Rev.* 2020
- Courson, J. A., Landry, P. T., Do, T., Spehlmann, E., Lafontant, P. J., Patel, N., Rumbaut, R. E., & Burns, A. R. (2021). Serial Block-Face Scanning Electron Microscopy (SBF-SEM) of Biological Tissue Samples. Journal of Visualized Experiments, 169. https://doi.org/10.3791/62045
- Deerinck, T., Bushong, E., Lev-Ram, V., Shu, X., Tsien, R., & Ellisman, M. (2010). Enhancing Serial Block-Face Scanning Electron Microscopy to Enable High Resolution 3-D Nanohistology of Cells and Tissues. Microscopy and Microanalysis, 16(S2), 1138–1139. https://doi.org/10.1017/S1431927610055170
- Gawish R, Starkl P, Pimenov L, Hladik A, Lakovits K, Oberndorfer F, Cronin SJ, Ohradanova-Repic A, Wirnsberger G, Agerer B, Endler L, Capraz T, Perthold JW, Cikes D, Koglgruber R, Hagelkruys A, Montserrat N, Mirazimi A, Boon L, Stockinger H, Bergthaler A, Oostenbrink C, Penninger JM, Knapp S. ACE2 is the critical in vivo receptor for SARS-CoV-2 in a novel COVID-19 mouse model with TNF- and IFNγ-driven immunopathology. Elife. 2022 Jan 13;11:e74623. doi: 10.7554/eLife.74623. PMID: 35023830; PMCID: PMC8776253.

- Gray, Henry; Standring, Susan; Anhand, Neel, eds. (2021). Gray's Anatomy: the anatomical basis of clinical practice (42nd ed.). Amsterdam: Elsevier. p. 1035. ISBN 978-0-7020-7705-0.
- H. Zhang, J.M. Penninger, Y. Li, N. Zhong, A.S. Slutsky Angiotensin-converting enzyme 2 (ACE2) as a SARS-CoV-2 receptor: molecular mechanisms and potential therapeutic target Intensive Care Med. (2020), pp. 1-5
- Haddad M, Sharma S. StatPearls [Internet]. StatPearls Publishing; Treasure Island (FL): Jul 20, 2023. Physiology, Lung.
- Hanada S, Pirzadeh M, Carver KY, Deng JC. Respiratory Viral Infection-Induced Microbiome Alterations and Secondary Bacterial Pneumonia. Front Immunol 2018;9:2640
- Hu G, Christman JW. Editorial: Alveolar Macrophages in Lung Inflammation and Resolution. Front Immunol. 2019 Sep 24;10:2275. doi: 10.3389/fimmu.2019.02275. PMID: 31616438; PMCID: PMC6768960.
- Invernizzi R., Lloyd C.M., Molyneaux P.L. Respiratory microbiome and epithelial interactions shape immunity in the lungs. *Immunology.* 2020;n/a(n/a).
- Jha NK, Ojha S, Jha SK, Dureja H, Singh SK, Shukla SD, Chellappan DK, Gupta G, Bhardwaj S, Kumar N, Jeyaraman M, Jain R, Muthu S, Kar R, Kumar D, Goswami VK, Ruokolainen J, Kesari KK, Singh SK, Dua K. Evidence of Coronavirus (CoV) Pathogenesis and Emerging Pathogen SARS-CoV-2 in the Nervous System: A Review on Neurological Impairments and Manifestations. J Mol Neurosci. 2021 Nov;71(11):2192-2209. doi: 10.1007/s12031-020-01767-6. Epub 2021 Jan 19. PMID: 33464535; PMCID: PMC7814864.
- Khan YS, Lynch DT. Histology, Lung. [Updated 2023 May 1]. In: StatPearls [Internet]. Treasure Island (FL): StatPearls Publishing; 2024 Jan-.
- Khaswal A, Kumar V, Kumar S. Long-Term Health Consequences of SARS-CoV-2: Assumptions Based on SARS-CoV-1 and MERS-CoV Infections. Diagnostics (Basel). 2022 Jul 31;12(8):1852. doi: 10.3390/diagnostics12081852. PMID: 36010203; PMCID: PMC9406530.
- Li X., Geng M., Peng Y., Meng L., Lu S. Molecular immune pathogenesis and diagnosis of COVID-19. *J Pharm Anal.* 2020;10(2):102–108.

- Li Y, Fu L, Gonzales DM, Lavi E (2004) Coronavirus neurovirulence correlates with the ability of the virus to induce proinflammatory cytokine signals from astrocytes and microglia. J Virol 78(7):3398–3406
- Li Y, Wang M, Zhou Y, Chang J, Xian Y, Mao L (2020). Acute Cerebrovascular Disease Following COVID-19: A Single Center, Retrospective, Observational Study. SSRN 2020; Available at SSRN: https://ssrn.com/abstract=3550025
- Li Y, Wang M, Zhou Y, Chang J, Xian Y, Mao L (2020). Acute Cerebrovascular Disease Following COVID-19: A Single Center, Retrospective, Observational Study. SSRN 2020; Available at SSRN: https://ssrn.com/abstract=3550025
- Li YC, Bai W, Hashikawa T (2020) The neuroinvasive potential of SARS-CoV2 may be at least partially responsible for the respiratory failure of COVID-19 patients. J Med Virol 92(6):552–555
- Lloyd C.M., Marsland B.J. Lung homeostasis: influence of age, microbes, and the immune system. *Immunity.* 2017;46(4):549–561.
- Maina, J. and West, J. (2005). Thin and strong! the bioengineering dilemma in the structural and functional design of the blood-gas barrier. Physiological Reviews, 85(3), 811-844. https://doi.org/10.1152/physrev.00022.2004
- Mammoto A, Mammoto T. Vascular Niche in Lung Alveolar Development, Homeostasis, and Regeneration. Front Bioeng Biotechnol. 2019 Nov 12;7:318. doi: 10.3389/fbioe.2019.00318. PMID: 31781555; PMCID: PMC6861452.
- Mao L, Jin H, Wang M, Hu Y, Chen S, He Q, Chang J, Hong C, Zhou Y, Wang D, Miao X, Li Y, Hu B. Neurologic Manifestations of Hospitalized Patients With Coronavirus Disease 2019 in Wuhan, China. JAMA Neurol. 2020 Jun 1;77(6):683-690. doi: 10.1001/jamaneurol.2020.1127. PMID: 32275288; PMCID: PMC7149362.
- Middleton EA, Weyrich AS, Zimmerman GA. Platelets in Pulmonary Immune Responses and Inflammatory Lung Diseases. Physiol Rev. 2016 Oct;96(4):1211-59. doi: 10.1152/physrev.00038.2015. Epub 2016 Aug 3. PMID: 27489307; PMCID: PMC6345245.
- Montoya-Navarrete AL, Guerrero-Barrera AL, Quezada-Tristán T, Valdivia-Flores AG, Cano-Rábano MJ. Red blood cells morphology and morphometry in adult, senior, and geriatricians dogs by optical and scanning electron microscopy. Front Vet Sci. 2022 Nov 10;9:998438. doi: 10.3389/fvets.2022.998438. PMID: 36439358; PMCID: PMC9685804.

- Mous, D., Kool, H., Wijnen, R., Tibboel, D., & Rottier, R. (2018). Pulmonary vascular development in congenital diaphragmatic hernia. European Respiratory Review, 27(147), 170104. https://doi.org/10.1183/16000617.0104-2017
- Naeem A, Rai SN, Pierre L. Histology, Alveolar Macrophages. [Updated 2022 Oct 10]. In: StatPearls [Internet]. Treasure Island (FL): StatPearls Publishing; 2024 Jan-. Available from: https://www.ncbi.nlm.nih.gov/books/NBK513313/
- Naeem A, Rai SN, Pierre L. Histology, Alveolar Macrophages. 2022 Oct 10. In: StatPearls [Internet]. Treasure Island (FL): StatPearls Publishing; 2024 Jan–. PMID: 30020685.
- Nicod L.P. Lung defences: an overview. *Eur Respir Rev.* 2005;14(95):45–50.
- Patel, N. and Patel, K. (2023). Estimation of pulmonary gas exchange in the human respiratory system under normal and abnormal conditions. Biosciences Biotechnology Research Asia, 20(1), 255-262. https://doi.org/10.13005/bbra/3086
- Peddie, C. J., & Collinson, L. M. (2014). Exploring the third dimension: Volume electron microscopy comes of age. Micron, 61, 9–19. https://doi.org/10.1016/j.micron.2014.01.009
- Platelets in Pulmonary Immune Responses and Inflammatory Lung Diseases Elizabeth A. Middleton, Andrew S. Weyrich, and Guy A. Zimmerman Physiological Reviews 2016 96:4, 1211-1259
- Pormohammad A, Ghorbani S, Khatami A, Farzi R, Baradaran B, Turner DL, Turner RJ, Bahr NC, Idrovo JP. Comparison of confirmed COVID-19 with SARS and MERS cases - Clinical characteristics, laboratory findings, radiographic signs and outcomes: A systematic review and meta-analysis. Rev Med Virol. 2020 Jul;30(4):e2112. doi: 10.1002/rmv.2112. Epub 2020 Jun 5. PMID: 32502331; PMCID: PMC7300470.
- Roujian Lu, Xiang Zhao, Juan Li, Peihua Niu, Bo Yang, Honglong Wu, Wenling Wang, Hao Song, Baoying Huang, Na Zhu, Yuhai Bi, Xuejun Ma, Faxian Zhan, Liang Wang, Tao Hu, Hong Zhou, Zhenhong Hu, Weimin Zhou, Li Zhao, Jing Chen, Yao Meng, Ji Wang, Yang Lin, Jianying Yuan, Zhihao Xie, Jinmin Ma, William J Liu, Dayan Wang, Wenbo Xu, Edward C Holmes, George F Gao, Guizhen Wu, Weijun Chen, Weifeng Shi, Wenjie Tan,Genomic characterisation and epidemiology of 2019 novel coronavirus: implications for virus origins and receptor binding,The Lancet,Volume 395, Issue 10224,2020,Pages 565574,ISSN01406736,https://doi.org/10.1016/S01406736(20)302518.(https://www.sciencedirect.com/science/article/pii/S0140673620302518)

- Schupp JC, Adams TS, Cosme C Jr, Raredon MSB, Yuan Y, Omote N, Poli S, Chioccioli M, Rose KA, Manning EP, Sauler M, DeIuliis G, Ahangari F, Neumark N, Habermann AC, Gutierrez AJ, Bui LT, Lafyatis R, Pierce RW, Meyer KB, Nawijn MC, Teichmann SA, Banovich NE, Kropski JA, Niklason LE, Pe'er D, Yan X, Homer RJ, Rosas IO, Kaminski N. Integrated Single-Cell Atlas of Endothelial Cells of the Human Lung. Circulation. 2021 Jul 27;144(4):286-302. doi: 10.1161/CIRCULATIONAHA.120.052318. Epub 2021 May 25. PMID: 34030460; PMCID: PMC8300155.
- Shereen M.A., Khan S., Kazmi A., Bashir N., Siddique R. COVID-19 infection: origin, transmission, and characteristics of human coronaviruses. *J Adv Res.* 2020;24:91–98
- Stereology: a bridge to a better understanding of lung structure and function V. Brusasco, A. T. Dinh-Xuan European Respiratory Journal Mar 2010, 35 (3) 477-478; **DOI:** 10.1183/09031936.00005710
- Sun C, Han Y, Zhang R, Liu S, Wang J, Zhang Y, Chen X, Jiang C, Wang J, Fan X, Wang J. Regulated necrosis in COVID-19: A double-edged sword. Front Immunol. 2022 Aug 25;13:917141. doi: 10.3389/fimmu.2022.917141. PMID: 36090995; PMCID: PMC9452688.
- Tapia, J. C., Kasthuri, N., Hayworth, K. J., Schalek, R., Lichtman, J. W., Smith, S. J., & Buchanan, J .(2012). High-contrast en bloc staining of neuronal tissue for field emission scanning electron microscopy. Nature Protocols, 7(2), 193–206. https://doi.org/10.1038/nprot.2011.439
- Terry, P. and Traystman, R. (2016). The clinical significance of collateral ventilation. Annals of the American Thoracic Society, 13(12), 2251-2257. https://doi.org/10.1513/annalsats.201606-448fr
- Thon JN, Italiano JE. Platelets: production, morphology and ultrastructure. Handb Exp Pharmacol. 2012;(210):3-22. doi: 10.1007/978-3-642-29423-5_1. PMID: 22918725.
- Totura A.L., Baric R.S. SARS coronavirus pathogenesis: host innate immune responses and viral antagonism of interferon. *Curr Opin Virol.* 2012;2(3):264–275.
- Turgeon ML (2004). Clinical Hematology: Theory and Procedures. Lippincott Williams & Wilkins. p. 100. ISBN 9780781750073.

- Wan Y., Shang J., Graham R., Baric R.S., Li F. Receptor recognition by the novel coronavirus from wuhan: an analysis based on decade-long structural studies of SARS coronavirus. *J Virol.* 2020;94(7)
- Weinberger SE, Cockrill BA, Mandel J (2019). Principles of pulmonary medicine (Seventh ed.). Philadelphia, PA. pp. 288–289. ISBN 978-0-323-52373-8. OCLC 1020498796.
- WHO COVID-19 Dashboard. Geneva: World Health Organization, 2020. Available online: https://covid19.who.int/ (last cited: [7.11.2023]).
- Yan W, Zheng Y, Zeng X, He B, Cheng W. Structural biology of SARS-CoV-2: open the door for novel therapies. Signal Transduct Target Ther. 2022 Jan 27;7(1):26. doi: 10.1038/s41392-022-00884-5. PMID: 35087058; PMCID: PMC8793099. doi: 10.1038/s41392-022-00884-5
- Yang, H., Rao, Z. Structural biology of SARS-CoV-2 and implications for therapeutic development. Nat Rev Microbiol 19, 685–700 (2021). https://doi.org/10.1038/s41579-021-00630-8
- Yu Lung Lau, JS Malik Peiris,Pathogenesis of severe acute respiratory syndrome,Current Opinion in Immunology,Volume 17, Issue 4,2005,Pages 404-410,ISSN 09527915,https://doi.org/10.1016/j.coi.2005.05.009.(https://www.sciencedirect.com/science/article/pii/S0952791505000750)